Genetically Encoded and Modular SubCellular Organelle Probes (GEM-SCOPe) reveal lysosomal and mitochondrial dysfunction driven by *PRKN* knockout

Camille Goldman[1-5], Tatyana Kareva[1-5], Lily Sarrafha[1-5], Braxton R. Schuldt[1-5], Abhishek Sahasrabudhe[1-3], Tim Ahfeldt[1-5 **], Joel W. Blanchard[1-6 *]

1. Icahn School of Medicine, Mount Sinai, New York, NY, USA
2. Nash Family Department of Neuroscience, Mount Sinai, New York, NY, USA
3. Friedman Brain Institute, Mount Sinai, New York, NY, USA
4. Ronald M. Loeb Center for Alzheimer's Disease, Mount Sinai, New York, NY USA
5. Black Family Stem Cell Institute, Mount Sinai, New York, NY, USA
6. Lead Contact

* Corresponding author

** 2nd corresponding author

Correspondence: joel.blanchard@mssm.edu

Correspondence: ahfeldt@gmail.com

Summary

Cellular processes including lysosomal and mitochondrial dysfunction are implicated in the development of many diseases. Quantitative visualization of mitochondria and lysosoesl is crucial to understand how these organelles are dysregulated during disease. To address a gap in live-imaging tools, we developed GEM-SCOPe (Genetically Encoded and Modular SubCellular Organelle Probes), a modular toolbox of fluorescent markers designed to inform on localization, distribution, turnover, and oxidative stress of specific organelles. We expressed GEM-SCOPe in differentiated astrocytes and neurons from a human pluripotent stem cell *PRKN*-knockout model of Parkinson's disease and identified disease-associated changes in proliferation, lysosomal distribution, mitochondrial transport and turnover, and reactive oxygen species. We demonstrate GEM-SCOPe is a powerful panel that provide critical insight into the subcellular mechanisms underlying Parkinson's disease in human cells. GEM-SCOPe can be expanded upon and applied to a diversity of cellular models to glean an understanding of the mechanisms that promote disease onset and progression.

Keywords

Live-cell imaging, induced pluripotent stem cells, Parkinson's Disease, astrocytes, PRKN

Introduction

Parkinson's Disease (PD) is a common neurodegenerative disease that robs individuals of their motor and cognitive functions, affecting over 10 million people worldwide and with an estimated 90,000 new diagnoses in the United States each year[1]. PD is clinically characterized by bradykinesia, resting tremor, rigidity, and postural instability[2-5] and pathologically characterized by the loss of dopaminergic neurons in the substantia nigra pars compacta and buildup of intracellular deposits of α-synuclein into insoluble protein aggregates called Lewy Bodies[2,6-8]. From the first pathological descriptions of PD in the mid-20th century, advancements in many fields, including histology, genetics, cell biology, and neurology enabled insight into many aspects of the disease, from determining genetic and environmental risk factors and mapping disease progression to identifying pathways and proteins to target therapeutically. Despite great progress, there is still incomplete understanding of the cellular dysfunction that precedes and contributes to chronic neuronal death.

This limited advancement arises in part due to the absence of tools used to track molecular and cellular changes in real-time throughout disease progression. Studies on human post-mortem brain tissue are largely representative of end-stage disease states, making it difficult to dissect which phenotypes are a primary, causative effect and which phenotypes are a secondary response[9]. Mouse models offer more opportunities to study multiple time points throughout disease progression as motor and cognitive symptoms can be monitored over time. However, targeting specific cell types in mice remains technically challenging and time-consuming.

53 Emerging technologies such as the miniscope allow continuous monitoring of fluorescence-based
54 readouts on a cellular level in live mouse and rat brains[10-12]. However, the type of readout from
55 the miniscope has been restricted to neuronal activity from fluorescent calcium sensors and
56 resolution along the z-axis remains a limiting factor in analyzing deeper cortical tissue.

57 Regardless of such technologies, current genetic rodent models of PD fail to completely
58 recapitulate human disease and lack key pathological hallmarks. Drug-induced models can
59 recapitulate late-stage disease phenotypes and behaviors, but due to their acute onset, are
60 inadequate to study the gradual accumulation of cellular dysfunction that precedes clinical
61 presentation[13,14]. Advancements in induced pluripotent stem cell (iPSC) differentiation and
62 CRISPR/Cas9 genome editing have led to the emergence of genetic cellular models of PD[15-18].
63 These models enable researchers to study the effects of genetic and environmental factors on
64 specific human cell populations relevant to PD.

65 Cellular models of PD provide an exciting opportunity to study subcellular changes and responses
66 to stress or treatment in live cells. Cells can be genetically engineered to express fluorescent
67 proteins that can then be visualized by microscopy in live cells. The applicability of GFP as a
68 reporter gene was immediately appreciated after its identification and isolation in 1962[19]. Since
69 then, hundreds of fluorophores have been developed by introducing mutations to naturally
70 occurring fluorophores isolated from sea anemones and jellyfish to modulate fluorescence
71 intensity, half-life, and excitation/emission spectra[20]. Additional fluorophores have been
72 developed as biosensors, by fluorescing or changing fluorescence emission in the presence of a
73 certain ligand or under specific cellular conditions[20-25]. Cells can express these fluorophores with
74 virtually limitless possibilities with regards to subcellular localization, cell-type specific expression,
75 and temporally controlled expression. Genetically encoded fluorescent proteins can be used to
76 follow a population of cells as they change due to aging, genetics, or environmental stressors and
77 stimuli.

78 PD has a complex genetic architecture underlying the disease. Over 90% of PD cases are
79 idiopathic; over 90 genetic risk loci have been identified by GWAS, but any of those individual
80 variants confer little risk on their own[26]. The remaining 10% of PD cases can be linked to highly
81 penetrant mutations in a handful of genes. While extremely rare, studying the function of these
82 genes and their impact on cellular processes sheds light on the fundamental pathways that drive
83 PD pathogenesis. Here, we focus on the *PRKN* gene. Autosomal recessive loss of function
84 mutations in *PRKN* are the most frequent known genetic cause of early onset cases of PD,
85 accounting for about 15% of PD cases with onset before the age of 50[27-30]. *PRKN* encodes for
86 the protein PRKN, an E3 ubiquitin ligase associated with mitochondria. PRKN directs the
87 ubiquitination of outer mitochondrial membrane proteins on damaged mitochondria, targeting
88 them for degradation via the autophagy-lysosomal pathway (mitophagy)[31-33]. While the function
89 of PRKN is well understood, it is still unclear how loss of PRKN function leads to the gradual
90 disease progression of early onset PD. It is believed that neurodegeneration can begin over 20
91 years before clinical onset, with a prolonged prodromal phase associated with several non-motor
92 symptoms. Thus, it is crucial to study models of early disease to understand what cellular
93 disturbances in the prodromal phase culminate in neurodegeneration.

94 Here, we present GEM-SCOPe (**G**enetically **E**ncoded and **M**odular **S**ub**C**ellular **O**rganelle
95 **P**robes), an expandable panel of genetically encoded reporters to track and quantify the
96 subcellular phenotypes in live cells. We developed a library of constructs that localize specifically
97 to the nucleus, mitochondria, and lysosomes and included fluorophores with a variety of emission
98 spectra or biosensor capabilities. All the lentiviral constructs were developed in the same
99 backbone vector to be modular, enabling any component, be it promotor, localization signal,
100 fluorophore, or antibiotic resistance, to be easily removed or replaced. We validated the
101 fluorophores with live-imaging of human induced pluripotent stem cell (hiPSC)-derived midbrain
102 astrocytes employing existing chemical dyes and chemical perturbations. We then applied GEM-

103 SCOPe to hiPSC-derived astrocytes and neurons from a *PRKN*-knockout model of PD[15]. This
104 revealed previously unseen changes in cellular proliferation, lysosomal distribution, mitochondrial
105 motility and turnover, and reactive oxygen species production. Our results demonstrate the
106 widespread utility of GEM-SCOPe to study a variety of translationally important subcellular
107 changes affected during PD. The modular, combinatorial flexibility of GEM-SCOPe can be
108 adapted to investigate any disease, and, therefore, it is a critical new resource that can be broadly
109 applied in neurodegenerative research and beyond.

110

111 Results

112 Building a modular toolbox for the subcellular localization of 113 genetically encoded fluorophores

114 We developed GEM-SCOPe for live-cell imaging of subcellular organelle dynamics. We aimed to
115 produce a system that is highly modular to easily customize the expression, localization,
116 fluorescence, and selection for any given experimental need. We started with the FUW
117 backbone[34], a 3rd generation lentivirus backbone with a ubiquitin C promoter for high, ubiquitous
118 expression of the transgene across cell types[34,35] and a woodchuck hepatitis virus post-
119 transcriptional regulatory element (WPRE) for improved lentiviral expression[34,36,37]. The designed
120 lentiviral constructs contain four components: promoter, localization sequence, fluorophore, and
121 antibiotic resistance (**Fig. 1A**). The content of these four components can be mixed and matched
122 to generate a library of lentiviral constructs to fit a diverse field of experimental needs. To generate
123 constructs *de novo*, components were combined and inserted into the plasmid via Gibson
124 assembly (**Fig. 1B, top**). Restriction sites were kept between each domain, so each component
125 or group of components could be excised via restriction digest and replaced with a different

126 component, either by restriction site cloning or Gibson assembly (**Fig. 1B, bottom**). Thus, each
127 component of the lentiviral plasmid can be removed or replaced to accommodate features such
128 as cell-type specificity with cell-type specific promoters, alternative subcellular localization, and
129 unique fluorophores.

130 The FUW backbone has a ubiquitin C promoter, but this can be replaced with lineage or cell-type-
131 specific promoters for selective expression in specific cell types or with drug-inducible promoters
132 to temporally control when the construct is transcribed (**Fig. S1A**). Subcellular localization is
133 determined by including the whole or partial coding sequence of a peptide with a known and
134 specific subcellular localization. This domain can be omitted to produce a fluorophore expressed
135 in the cytoplasm. The fluorophore component of the construct offers the most flexibility, from basic
136 fluorescent proteins to more complex fluorophores that change fluorescent excitation and/or
137 emission wavelength with time or environment. All plasmids generated for GEM-SCOPe have
138 been deposited to Addgene(**Table S1**).

139 We developed GEM-SCOPe constructs to localize fluorophores to the cytoplasm (no tag), nucleus
140 (H2B-tag), mitochondria (COX8A-tag), and lysosome (LAMP1-tag) (**Fig. 1C**). Fluorophore
141 localization was validated using commercially available live cellular dyes. Nuclear localization was
142 achieved by fusing fluorophores to the C-terminus of histone 2B (H2B). H2B is an integral
143 chromatin protein that is found in all cells and is localized specifically to the nucleus[38,39]. H2B
144 fused to mTagBFP2, a blue fluorophore, (H2B-mTagBFP2) co-localizes with DRAQ5, a far-red
145 live-cell nuclear dye[40] (**Fig. 1C, top**; Mander's coefficient > 0.99±0.0001). In addition to the
146 mTagBFP2 construct, we also developed lentiviral plasmids with H2B fused to Emerald (green;
147 H2B-Emerald) and mCherry (red; H2B-mCherry) (**Fig. 1A, S1B**).

148 To localize fluorophores to the lysosome, we utilized the N-terminal peptide sequence of
149 lysosomal-associated membrane protein 1 (LAMP1), a major component of lysosomal
150 membranes that plays a key role in lysosomal biogenesis and homeostasis. The N-terminus of

151 LAMP1 fused to mCherry (LAMP1-mCherry) co-localizes with LysoTracker (Thermo Scientific)
152 (**Fig. 1C, middle**; Mander's coefficient = 0.92±0.03). LysoTracker is a fluorophore that is partially
153 protonated at neutral pH and can readily cross membranes; once protonated it can no longer
154 diffuse so the fluorescent signal gets trapped in acidic compartments, including, but not limited to,
155 the lysosome[41,42]. Overexpression of LAMP1 is associated with numerous cancers and cancer
156 metastasis[43-46]. By only using a partial sequence of LAMP1 and not the full peptide sequence, we
157 are able to target the fluorophore specifically to the lysosome without increasing the expression
158 of endogenous LAMP1 (**Fig. S1C**). We also developed lentiviral plasmids with the LAMP1
159 targeting sequence fused to Emerald (green; LAMP1-Emerald; **Fig. 1A, 1D**).

160 Finally, mitochondrial localization was achieved using the mitochondrial targeting sequence of
161 COX8A. COX8A is a nuclear-encoded subunit of cytochrome-c oxidase (Complex IV) in the
162 electron transport chain[47,48]. The first 25 amino acid residues of the COX8A peptide sequence
163 target the peptide to the mitochondrial inner membrane and are widely used to specifically localize
164 proteins and fluorophores to the mitochondria[49-51]. To confirm mitochondrial specificity of COX8A-
165 Emerald we compared localization with MitoTracker (Thermo Scientific), a dye that accumulates
166 in the mitochondria due to the negative membrane potential of the inner mitochondrial
167 membrane[41,52]. The mitochondrial targeting sequence fused to an Emerald fluorophore (COX8A-
168 Emerald) exhibited significant co-localization with MitoTracker (**Fig. 1C, bottom**; Mander's
169 coefficient = 0.97±0.003). We developed lentiviral plasmids with the COX8A targeting sequence
170 fused to mCherry (red; COX8A-mCherry; **Fig. 1A, 1D**), Timer (green/red; COX8A-Timer; **Fig. 1A,**
171 **Fig. 5**), and Lemon (cyan/yellow; COX8A-Lemon; **Fig. 1A, Fig. S2**).

172 Once the localization strategies were finalized, we swapped out the fluorophores with different
173 fluorescent proteins that are excited and emitted at alternative wavelengths. Mixing localization
174 sequences and fluorophores with unique emission spectra allows simultaneous imaging of
175 multiple sub-cellular processes in the same cells such as mitochondrial network and lysosomal

176 distribution (**Fig. 1D**). Utilizing a combination of subcellular localization and diverse fluorophores,
177 we developed GEM-SCOPe, a fluorescent, live-cell imaging toolbox of lentiviral constructs that
178 were systematically validated to quantify cellular proliferation, lysosomal distribution, and
179 mitochondrial dynamics in human Parkinson's disease astrocytes.

180

181 H2B-fused fluorophores offer improvements for efficiently 182 labelling nuclei for multi-day live-cell assays

183 Quantification of cellular phenotypes by fluorescence microscopy is dependent on normalization
184 to total cell number. This is often accomplished by counting the number of nuclei. A few fluorescent
185 dyes that can cross the cellular and nuclear membranes of live cells and bind specifically to DNA
186 are commercially available. While efficient for short-term and end-point assays, such dyes
187 intercalate in DNA and therefore have cytotoxic and mutagenic effects[53,54]. Furthermore, nuclear
188 dyes do not remain contained within the nuclear compartment, and their signal leaches into the
189 cytoplasm in just a few hours after exposing the cells. The cytotoxicity and loss of precise labeling
190 over time render these dyes less useful for long-term microscopy or cell-tracking experiments. To
191 address these concerns, we developed lentiviral constructs expressing nuclear-localized
192 fluorophores by fusing the nucleus-specific histone protein, H2B, with either mTagBFP2, Emerald,
193 or mCherry (**Fig. 1C, 2A**). Human induced pluripotent stem-cell (hiPSC)-derived astrocytes
194 transfected with H2B-mTagBFP2 were co-stained with DRAQ5, a far-red DNA-stain for live cells.
195 The localization of the two nuclear signals was compared 1 hours and 24 hours after the addition
196 of DRAQ5. Immediately after adding DRAQ5, there was no difference between the DRAQ5 stain
197 and the H2B-mTagBFP2 (2-way ANOVA with Tukey's HSD; adj-p = 0.83) (**Fig. 2B, C**). Over the
198 experimental period, the DRAQ5 signal spread significantly (26±5% extranuclear; adj-p < 0.0001),
199 while the extranuclear H2B-mTagBFP2 signal did not significantly change (adj-p = 0.99) (**Fig. 2B,**

200 **C**). While the human eye can still readily distinguish the nucleus from the extranuclear stain in the
201 DRAQ5 images, image analysis programs that rely on grey values for segmentation often fail to
202 correctly differentiate the true nuclear signal from the extranuclear signal. Thus, lentiviral
203 constructs expressing nuclear-localized fluorophores, such as the demonstrated H2B-
204 mTagBFP2, can provide better alternatives for long-term live-imaging experiments with multiple
205 time points.

206

207 H2B-fused fluorophores reveal increased cellular
208 proliferation in PRKN knockout astrocytes

209 While dopaminergic neuron death is the predominant cellular outcome in Parkinson's Disease
210 (PD), other cell types in the brain may change cell cycle regulation under neurotoxic conditions.
211 Tracking cell numbers to monitor proliferation, senescence, or death in vitro can help researchers
212 understand how different cell populations are responding to neurotoxic stress or potential
213 therapeutic strategies.

214 First, we validated that our nuclear-localized construct, H2B-Emerald, could be used to track
215 cellular proliferation. The proliferation of H2B-Emerald transduced hiPSC-derived astrocytes was
216 induced using fetal bovine serum (FBS) or blocked by inhibiting the proteasome with MG-132.
217 Astrocyte proliferation was measured by changes in the number of H2B-Emerald nuclei. As
218 expected, the astrocytes treated with FBS proliferated twice as rapidly as the untreated astrocytes
219 over 48 hours (2-way ANOVA with Tukey's HSD, p-adj = 0.005, **Fig. S3**), while the astrocytes
220 treated with MG-132 did not significantly proliferate over the same period (adj-p = 0.08, **Fig. S3**).
221 Thus, the GEM-SCOPe H2B-fluorophore fusion proteins can be used to track cellular proliferation
222 over multiple days in live cell cultures.

223 To examine the effect of loss of *PRKN* on astrocyte proliferation, we transduced wild-type
224 (*PRKN*$^{+/+}$) astrocytes with H2B-Emerald and isogenic *PRKN* knockout (*PRKN*$^{-/-}$) astrocytes with
225 H2B-mCherry (**Fig. 2D**). Leveraging the modularity of GEM-SCOPe, we were able to mix the two
226 astrocyte populations together and track their proliferation simultaneously. Over 48 hours, the
227 *PRKN*$^{-/-}$ population increased significantly (2-way ANOVA with Tukey's HSD, p-adj = 0.03; **Fig.**
228 **2E, F**) while the *PRKN*$^{+/+}$ population did not proliferate in the same period (2-way ANOVA with
229 Tukey's HSD, p-adj = 0.4; **Fig. 2E, F**). These results contradict mouse studies that found that
230 PRKN-null mice had decreased astroglia proliferation[55]. However, PRKN has also been described
231 as a tumor suppressor, with loss of function mutations arising in a variety of cancers, including
232 glioblastomas[56-58]. Studies on PRKN in the context of cancer find that cancer regulates the
233 degradation of cyclins and cyclin-dependent kinases involved in the G1/S transition, thus
234 promoting continued proliferation[57,59,60]. It has been hypothesized that the outcome of loss of
235 function PRKN mutations are highly cell-context dependent; the increased half-life of cyclins leads
236 to cancer in mitotically competent cells while the same cyclins promote apoptosis upon cell cycle
237 reentry in post-mitotic neurons[57,61-64]. Our findings highlight the importance of studying disease-
238 relevant human cells to capture the intricacies and nuances specific to the human brain that could
239 contribute to PD.

240

241 LAMP1-localized fluorophores reveal changes in lysosomal
242 distribution in response to chemical and genetic stressors

243 Lysosomal dysfunction is widely implicated in PD and other forms of neurodegeneration. Several
244 PD-risk and familial genes are involved in the autophagy-lysosomal-endosomal pathway[65-67], and
245 many hallmarks of lysosomal dysfunction associated with familial PD are present in idiopathic PD
246 [66,68,69]. Disruption to the autophagy-lysosomal-endosomal pathway is of broad importance in PD

247 and there is a crucial need to study lysosomal function and dysfunction in the context of PD
248 pathogenesis. As described above, we fused the N-terminus of LAMP1 to a fluorophore (Emerald
249 or mCherry) to specifically target the fluorescent signal to the lysosome (**Fig. 1C, 3A**). To validate
250 the GEM-SCOPe LAMP1-mCherry signal responds to lysosomal stress, hiPSC-derived
251 astrocytes transduced with LAMP1-mCherry lentivirus were exposed to bafilomycinA1 (BafA1) for
252 15 hours. BafA1 inhibits lysosomal proton pump V-ATPases, which blocks autophagosome-
253 lysosome fusion and lysosomal acidification, impairing lysosomal function [70,71]. hiPSC-derived
254 astrocytes were simultaneously transduced with a non-localized Emerald fluorophore lentivirus,
255 to provide a cell body marker. We used CellProfiler [72] to evaluate the lysosomal number, size, and
256 distribution within each cell. Compared to vehicle (DMSO) treatment, treatment with BafA1
257 increased the number of LAMP1-mCherry vesicles (unpaired t-test, $p = 0.04$; **Fig. 3B, C**), but did
258 not affect lysosome size (unpaired t-test, $p = 0.16$, **Fig. 3B, C**). Treatment with BafA1 altered the
259 distribution of lysosomes within the astrocytes. Astrocytes treated with BafA1 had a more
260 dispersed distribution of LAMP1-mCherry signal, with only 41±4% concentrated in the perinuclear
261 area, in contrast to 65±8% in vehicle-treated astrocytes (unpaired t-test, $p = 0.002$; **Fig. 3B, C**).
262 Perinuclear and juxtanuclear lysosomes have been posited to be more acidic than peripheral
263 lysosomes[73]. Lysosomal distribution can also be affected by cytosolic pH, with acidification
264 promoting the spreading of lysosomes away from the nucleus[74-76]. Since BafA1 inhibits V-
265 ATPases responsible for establishing and maintaining lysosomal pH, the redistribution of
266 lysosomes away from the nucleus upon BafA1 treatment might reflect a change in lysosomal or
267 cytosolic pH, and therefore lysosomal function, in the treated astrocytes.

268 In addition to its role in ubiquitinating damaged mitochondria for degradation via the autophagy-
269 lysosomal pathway[31-33], PRKN has been shown to regulate endosome organization[77] and
270 mitochondria-lysosome contact sites. Although it has been reported that *PRKN* knockout in
271 hiPSC-derived dopaminergic neurons leads to an increase in lysosome number and size

272 compared to isogenic, wild-type dopaminergic neurons[78], the effect of *PRKN* knockout on
273 lysosomes on human astrocytes is largely unknown. Due to PRKN's role in regulating the
274 autophagy-lysosomal pathway, we hypothesized *PRKN*$^{-/-}$ in human astrocytes would disrupt
275 lysosomal dynamics. To test this hypothesis, we applied the same CellProfiler analysis on
276 *PRKN*$^{+/+}$ and *PRKN*$^{-/-}$ hiPSC-derived astrocytes transduced with GEM-SCOPe Emerald and
277 LAMP1-mCherry lentivirus. *PRKN*$^{-/-}$ astrocytes had half as many LAMP1-mCherry vesicles per
278 cell compared to *PRKN*$^{+/+}$ astrocytes (unpaired t-test, p = 0.003, **Fig. 3D, E**). Additionally, the
279 *PRKN*$^{-/-}$ lysosomes were smaller than the *PRKN*$^{+/+}$ lysosomes (unpaired t-test, p = 0.055, **Fig. 3D,**
280 **E**). Finally, the *PRKN*$^{-/-}$ astrocytes had a decrease in perinuclear LAMP1-mCherry, with only
281 38±4% of LAMP1-mCherry signal located in the perinuclear area, compared to 45±3% in
282 *PRKN*$^{+/+}$ (unpaired t-test, p = 0.005, **Fig. 3D, E**). Our results utilizing our GEM-SCOPe LAMP1-
283 mCherry fluorophore suggest that lysosomal distribution in astrocytes is altered upon loss of
284 *PRKN* and further studies to examine lysosomal content and activity are needed to understand
285 the implications and how this could differ from observations in other cell types.

286

287 Mitochondria-localized fluorophores capture mitochondrial 288 fragmentation and alterations in mitochondrial trafficking 289 along PRKN knockout dopaminergic neuron axons

290 Much like lysosomal dysfunction, mitochondrial dysfunction is implicated in PD and
291 neurodegeneration. Therefore, monitoring mitochondrial network dynamics in response to stimuli
292 and stress is important in understanding neurodegenerative diseases. As described above, we
293 fused the N-terminus of the mitochondrial protein COX8A to a fluorophore (Emerald or mCherry)
294 to localize the fluorophore specifically to the mitochondria (**Fig. 1C, 4A**). To validate that GEM-

295 SCOPe COX8A localized fluorophores reflect changes to mitochondrial morphology, we induced
296 mitochondrial stress by treating hiPSC-derived astrocytes transduced with the COX8A-mEmerald
297 lentivirus with 2μM oligomycin for 4 hours. Mitochondrial stress induces fragmentation of the
298 mitochondrial network, which facilitates mitophagy, but also decreases mitochondrial network
299 respiratory capacity[79,80]. Oligomycin, an inhibitor of ATP synthase, is a known inducer of
300 mitochondrial fragmentation. Treatment with oligomycin induced mitochondrial fragmentation
301 when compared to vehicle-treated astrocytes. The average area of mitochondria was reduced
302 from 1.04 μm^2 in vehicle-treated astrocytes to 0.8 μm^2 in oligomycin-treated astrocytes (1-way
303 ANOVA with Dunett's Test, p-adj = 0.0002; **Fig. 4B, C left)**, and average branch length was
304 reduced from 1.28 μm in vehicle-treated astrocytes to 0.9 μm in oligomycin treated astrocytes (1-
305 way ANOVA with Dunett's Test, p-adj < 0.0001; **Fig. 4B, C middle)**, as expected from a more
306 fragmented mitochondrial network. The aspect ratio is the ratio of the mitochondrial length to
307 width. An aspect ratio of 1 indicates a perfect circle, while larger aspect ratios indicate longer and
308 narrower shapes. The mean aspect ratio decreased from 2.52 in vehicle-treated astrocytes to
309 2.14 in oligomycin-treated astrocytes (1-way ANOVA with Dunett's Test, p-adj < 0.0001; **Fig. 4B,**
310 **C right**), another indicator that mitochondria are fragmenting upon oligomycin treatment. Metrics
311 of mitochondrial network fragmentation (mitochondrial area, branch length, and aspect ratio) are
312 all affected in a dose-dependent manner, with increasing concentrations of oligomycin having
313 increasingly more severe effects on mitochondrial network fragmentation (**Fig. S4**).

314 The transport of mitochondria along neuronal axons is critical for proper synaptic function and
315 neurotransmitter release. We hypothesized *PRKN*$^{-/-}$ may impair axonal mitochondrial transport.
316 To investigate this hypothesis, we transduced wild-type (*PRKN*$^{+/+}$) and *PRKN* knock-out (*PRKN*$^{-/-}$
317) hiPSC-derived midbrain organoids with COX8A-mEmerald. To facilitate imaging of axonal
318 mitochondrial transport, we generated radial axonal arbors by splatting organoids onto the surface
319 of a plate and allowing the axons to grow out[81]. On day 164 of organoid differentiation, fluorescent

320 mitochondria were imaged at high magnification over several minutes to monitor the movement
321 of mitochondria along these axons (**Fig. 4D; Video S1**). In the anterograde direction (moving
322 away from the soma), *PRKN*$^{-/-}$ mitochondria moved only 20% of the distance covered by *PRKN*$^{+/+}$
323 mitochondria (Welch's t-test, $p < 0.0001$, **Fig. 4E left**) and took 50% longer (unpaired t-test, $p =$
324 0.005; **Fig. 4E right**). Retrograde-moving mitochondria moved the same distance (unpaired t-
325 test, $p = 0.59$, **Fig. 4F left)** but the *PRKN*$^{-/-}$ mitochondria moved for 150% longer compared to the
326 *PRKN*$^{+/+}$ mitochondria (Welch's t-test, $p = 0.02$; **Fig. 4F right**). PRKN has previously been
327 implicated in mitochondrial transport due to its ubiquitination of mitochondrial motor adaptor
328 complexes[82]. Our results demonstrate that PRKN loss of function impairs mitochondrial trafficking
329 in human neurons, likely reducing the delivery of functional mitochondria synaptic extremities and
330 ultimately compromising neuronal function.

331 Dynamic fluorophores measure deficiencies in mitochondrial 332 turnover and glutathione reduction potential in PRKN- 333 knockout astrocytes

334 We demonstrated the utility of single excitation and emission wavelengths to discern phenotypes
335 regarding cellular and subcellular dynamics. Numerous groups have developed fluorophores that
336 change emission wavelengths under certain conditions or circumstances. We introduced several
337 multi-emission fluorophores into GEM-SCOPe to enable quantification of organelle turnover,
338 acidification, and oxidation, in addition to the localization information described with the previous
339 fluorophores.

340 Fluorescent Timer is a mutated dsRed protein that irreversibly shifts its fluorescence emission
341 from green to red due to tyrosine oxidation and can be used as a molecular clock to track protein
342 turnover (**Fig. 5A**).[22] We, therefore, localized GEM-SCOPe-Timer to the mitochondria (COX8A-

343 Timer), to further investigate mitochondrial turnover[83,84] (**Fig. 5B**). To first validate COX8A-Timer,
344 mitophagy was inhibited by treating hiPSC-derived astrocytes transduced with COX8A-Timer with
345 the V-ATPase inhibitor bafilomycinA1 (BafA1). BafA1 treatment led to a significant increase in the
346 ratio of red-fluorescent mitochondria over green-fluorescent mitochondria compared to vehicle
347 control astrocytes (unpaired t-test, $p < 0.0001$; **Fig. 5C, D**). Since mitochondrial degradation and
348 turnover occur primarily through mitophagy, inhibition of mitophagy and mitochondrial recycling
349 via BafA1 treatment results in a predicted increase in longer-lived mitochondria.

350 Because PRKN is directly involved in mitophagy, and we observed impaired retrograde
351 mitochondrial transport in *PRKN*$^{-/-}$ neurons, we wanted to measure changes in mitochondrial
352 turnover in human *PRKN*$^{-/-}$ cells. We transduced wild-type (*PRKN*$^{+/+}$) and *PRKN* knockout *(PRKN*$^{-}$
353 $^{/-}$) hiPSC-derived astrocytes with GEM-SCOPe COX8A-Timer. The ratio of red-fluorescent signal
354 over green-fluorescent signal significantly increased in *PRKN*$^{-/-}$ astrocytes compared to *PRKN*$^{+/+}$
355 astrocytes (unpaired t-test, $p = 0.026$, **Fig. 5E, F**). When broken down by individual channel, there
356 was no change in the green fluorescence (2-way ANOVA with Sidak correction, p-adj = 0.1288,
357 **Fig. 5G**), indicating no change in mitochondrial biogenesis. The increase in red to green ratio was
358 driven by a significant increase in red-fluorescent signal (2-way ANOVA with Sidak correction, p-
359 adj = 0.0005, **Fig. 5G**), which is in concordance with an accumulation of older mitochondria due
360 to a failure to properly degrade mitochondria in the absence of PRKN.

361 An expected consequence of impaired mitochondrial recycling is an accumulation of damaged
362 mitochondria and an increase in mitochondria-associated reactive oxygen species (ROS) from
363 inefficient cellular respiration. To measure reactive oxygen levels in live astrocytes, we introduced
364 GRX1-roGFP2, an established fluorophore for measuring ROS, into GEM-SCOPe[25]. GRX1-
365 roGFP2 is a fusion protein between GRX1 and roGFP2. When GRX1 is oxidized by glutathione,
366 it can subsequently oxidize roGFP2. Oxidized roGFP2 shifts its emission spectrum from green
367 fluorescence to blue fluorescence (**Fig. 6A**)[25,85]. Thus, the ratio of green to blue fluorescence is

368 an indicator of glutathione oxidation state. When GRX1-roGFP2 is further coupled with a
369 mitochondrial localization sequence, we can measure the oxidative stress of the mitochondria.

370 This construct was available as a retroviral vector using the signal sequence from *Neurospora*
371 *crassa* ATP synthase protein 9[25]. When we cloned it into the FUW lentivirus backbone, we decided
372 to keep that localization sequence rather than replace it with the signal sequence for COX8A used
373 in the other GEM-SCOPe mitochondria-localized fluorophores (**Fig. 6B**). To validate GEM-SCOPe
374 GRX1-roGFP2 was working as expected, hiPSC-derived astrocytes transduced with mito-GRX1-
375 roGFP2 were treated with BafA1 to induce oxidative stress[86]. Astrocytes treated with BafA1 had
376 a significant decrease in the ratio of green fluorescence to blue fluorescence when compared to
377 vehicle (DMSO) treated astrocytes (unpaired t-test, $p < 0.0001$, **Fig. 6C, D**). The effect is driven
378 by a significant increase specifically in blue fluorescence (2-way ANOVA with Sidak correction, p-
379 adj < 0.0001, **Fig. 6E**) while the green fluorescence remained unchanged (2-way ANOVA with
380 Sidak correction, p-adj = 0.99, **Fig. 6E**). The increase in blue fluorescence is due to an increase
381 in roGFP2 oxidation, which is indicative of an increase in glutathione oxidation and the presence
382 of reactive oxygen species. Thus, GEM-SCOPe-mito-GRX1-roGFP can be used to monitor
383 glutathione reduction potential and how cells respond to reactive oxygen stress.

384 Because astrocytes play important metabolically supportive roles in the CNS and we observed
385 PRKN-related impairments to mitochondrial recycling with COX8A-Timer (**Fig. 5E-G**), we wanted
386 to understand if PRKN deficiency has effects on ROS production in astrocytes. We transduced
387 *PRKN*$^{+/+}$ and *PRKN*$^{-/-}$ astrocytes with mito-GRX1-roGFP2 lentivirus. Without introducing any
388 additional chemical mitochondrial stressors, we observed an siginificant reduction in the ratio of
389 green-fluorescence signal to blue-fluorescence signal in *PRKN*$^{-/-}$ compared to *PRKN*$^{+/+}$ astrocytes
390 (unpaired t-test, $p = 0.026$; **Fig. 6F, G**). This is indicative of an increase in ROS in *PRKN*$^{-/-}$
391 astrocytes which correlates with our other observation of decreased mitochondrial turnover in the
392 same cells. It has been previously demonstrated that *PRKN*$^{-/-}$ hiPSC-derived dopaminergic

393 neurons show increased cellular ROS[15] and *PRKN*$^{-/-}$ mice have decreased antioxidant capabilities
394 and increased ROS-related protein and lipid damage[87]. By introducing fluorophore-biosensors
395 into our lentiviral catalog, we were able to expand the phenotypes we can observe in live cells to
396 measure changes in the intracellular environment in response to chemical and genetic
397 perturbations.

398

399 Discussion

400 Here, we developed and validated GEM-SCOPe (Genetically Engineered, Modular, SubCellular
401 Organelle Probes), a collection of subcellularly targeted fluorophores encoded in a lentiviral
402 backbone. By exploiting the modular design of the constructs, we easily cloned fluorophores with
403 different excitation/emission spectra specified to localize to the nucleus, lysosomes, or
404 mitochondria. We demonstrated that these fluorophores specifically localize to the desired
405 organelle and can quantitatively assess cellular responses to chemical perturbations. Finally, we
406 applied GEM-SCOPe to human *PRKN*-knockout astrocytes and neurons, which revealed
407 widespread perturbations to cellular proliferation, lysosomal distribution, and mitochondrial
408 dynamics, providing new insights into PD pathogenesis.

409 Gliosis has been widely reported in human post-mortem brain studies of patients with *PRKN* loss-
410 of-function mutations[88-91]. Similar pro-inflammatory phenotypes have also been observed in
411 mouse models and stem-cell-derived glial models of PRKN deficiency[92,93]. However, there is still
412 a limited understanding of how genetic mutations related to PD modify astrocytes and their role
413 in neurodegeneration. We used GEM-SCOPe to investigate cellular, mitochondrial, and lysosomal
414 dynamics in astrocytes lacking functional PRKN protein. Using nucleus-localized fluorophores,
415 we show that *PRKN* knockout human astrocytes have increased cellular proliferation compared

416 to isogenic, wild-type astrocytes. LAMP1-localized fluorophores revealed that lysosomes in *PRKN*
417 knockout astrocytes are distributed further from the perinuclear nuclear area. Finally, a variety of
418 mitochondria-localized fluorophores revealed that *PRKN* knockout astrocytes have impaired
419 mitochondrial transport, decreased mitochondrial turnover, increased reactive oxygen species,
420 and oxidized glutathione. While additional experiments should be done to support these findings,
421 GEM-SCOPe highlights that there is extensive dysregulation and disruption to normal organelle
422 dynamics in human *PRKN* astrocytes that warrants further investigation.

423 GEM-SCOPe was developed in a 3rd generation lentiviral system. We selected this delivery
424 system because 1) lentiviruses are safe to produce; 2) they infect both dividing and non-dividing
425 cells; and 3) they can be used to develop stable cell lines. 3rd generation lentiviral systems are
426 replication-incompetent, so cells that are transduced with lentivirus cannot produce more viral
427 particles. Only the transfer plasmid, which contains the insert of interest, can be integrated into
428 the host genome; the other plasmids that encode lentiviral structural and envelope genes do not
429 integrate into the host genome, preventing viral replication. Most lentiviruses are produced with
430 VSV-G (Vesicular stomatitis virus G glycoprotein) as the envelope protein, as it provides broad
431 tropism and enables high transduction efficiency in a wide variety of cell types[94]. Finally, GEM-
432 SCOPe lentiviruses were developed with the option to include an antibiotic-resistance gene (**Fig.**
433 **1A**), which can be used to establish stable cell lines that have incorporated the lentiviral load.

434 Although lentiviruses provide a lot of flexibility and safety when delivering genetic information,
435 they also possess some limitations. Lentiviruses have an ideal plasmid size of 9-10kb, and viral
436 titer can decrease if plasmids exceed this size[95]. The H2B-mTagBFP2, H2B-mCherry, and H2B-
437 Emerald lentiviruses (**Fig. 1, 2**) are about 11kb each and transduced hiPSC-derived astrocytes
438 with about 90% efficiency. Coupled with the puromycin resistance that was also included in this
439 construct, we were still able to generate a population with 100% viral transduction despite the size
440 limitation. Another drawback of lentiviral gene delivery is that inserts often integrate into actively

441 transcribed loci[96]. Differentiation of hiPSCs into specific cell types requires extensive chromatin
442 remodeling, and genomic sequences integrated via lentivirus can often be silenced in this
443 process. In the case where hiPSCs must be transduced before differentiation, antibiotic selection
444 during differentiation can select for cells that have integrated the viral load into a genomic region
445 that is not silenced. The final drawback of lentiviral gene delivery is that fluorescence intensity is
446 dependent on the viral copy number in each cell and cannot be used as a readout for organelle
447 abundance. Rather, we need to use measurements like distribution, size, and ratios of different
448 emissions within the same cell. This is not just a limitation of lentiviral gene delivery but of other
449 viral and non-viral delivery systems.

450 In this study, we focused on PD and specifically the alterations to astrocytes with *PRKN* mutations.
451 However, alterations in proliferation, mitochondria, and lysosomes are by no means unique to PD.
452 Many reviews cover the extensive roles of mitochondria and lysosomes in health and disease[97-
453 100]. GEM-SCOPe can be applied beyond neuronal cells and neurodegeneration to countless other
454 cell types to investigate subcellular dynamics that affect disease development and progression.
455 Due to its modular design, GEM-SCOPe can be expanded and molded by research groups to
456 meet specific needs. Different targeting sequences can be integrated to localize fluorophores to
457 relevant subcellular compartments. New fluorophores and biosensors are always being
458 developed to measure additional intracellular conditions. By applying GEM-SCOPe to disease
459 models, we will be able to better understand how cells are disrupted over the course of disease
460 progression, providing insight for future therapeutic targets.

461

Acknowledgements

The authors thank Deanna Benson for discussions on mitochondrial transport and kymograph analysis. We thank the Microscopy CoRE at Icahn School of Medicine for providing access to the Leica DMi8 and Thermo Scientific CX7 High Content Screening Platform, as well as training and technical expertise for using these microscopes.

This work has been funded in part with federal funds from NASA under contract #80ARC022CA004 titled "Identification of Biomarkers and Pathological Mechanisms via Longitudinal Analysis of Neurological and Cerebrovascular Responses to Neurotoxic Stress Using a Multi-cellular Integrated Model of the Human Brain." This work was also supported by funding from Aligning Science Across Parkinsons (02663614), the NIH/NINDS (R010255E131 and UG3NS115064), and the CureAlz Fund. C.G. was supported by funding from the NIH/NIA (T32AG04968) and NIH/NINDS (F31NS13090), and L.S. was supported by the Training Program in Stem Cell Biology fellowship from the New York State Department of Health (NYSTEM-C32561GG).

Author Contributions

Conceptualization, C.G., T.A., and J.W.B.; Methodology, C.G., L.S., and T.A.; Validation, C.G.; Formal Analysis, C.G.; Investigation, C.G., T.K., L.S., and A.S.; Resources, C.G., T.K., L.S., and B.R.S.; Writing – Original Draft, C.G. and J.W.B.; Writing – Review & Editing, C.G., L.S., B.R.S., and J.W.B.; Visualization, C.G.; Funding Acquisition, T.A. and J.W.B.

483 # Declaration of Interests

484 The authors declare no competing interests

485 # Materials and Methods

486 ## Experimental model and study participant details

487 The human cell lines used in this study are detailed in the key resources table and below.

488 HEK293FT (RRID: CVCL_6911, fetal kidney origin, female sex) were maintained in DMEM (Gibco
489 10566) supplemented with 10% bovine calf serum (Cytiva SH30073) at 37 °C in a 5% CO2
490 incubator. Cells were passaged ever 4-5 days, when they reached 90% confluency.

491 H1(WA01) hESCs (male), BJ-SiPS-D iPSCs (male), and AG09173 iPSCs (female) were
492 maintained in StemFlex medium (Gibco A3349401) at 37 °C in a 5% CO2 incubator. Cells were
493 passaged every 3-4 days, when they reached 90% confluency. WA01 astrocytes were used for
494 all PRKN-genotype dependent experiments. BJ-SiPS-D and AG09173 were used for organelle
495 localization validation and chemical perturbation validation.

496

497 ## Molecular cloning

498 All vectors were derived from pFUW (Addgene plasmid #14882). pFUW was linearized using
499 NheI-HF (NEB R3131) and BamHI-HF (NEB R3136) per manufacturer's protocol, and the desired
500 fragment was gel-purified (Macherey-Nagel 740609). Components of the insert were PCR
501 amplified using Q5-Hot Start DNA Polymerase (NEB M0493) per manufacturer's
502 recommendations. Fluorophores were amplified from commercially available plasmids (see

503 Resource Table for complete list) and localization sequences were amplified from cDNA. Primers
504 were designed using the NEBuilder Assembly Tool (nebuilder.neb.com) to add 5' and 3'
505 sequences that make the fragments compatible for Gibson assembly and ordered from IDT
506 (Integrated DNA Technologies). Gibson reactions were set up with NEBuilder HiFi DNA Assembly
507 Master Mix (NEB E2621), 50ng of linearized backbone, and 3-fold molar excess of each PCR
508 fragment. For fragments less than 200bp, 5-fold molar excess was used. Reactions were
509 incubated at 50°C for 60 minutes. The Gibson product was transformed in 10-beta competent *E.*
510 *coli* (NEB C3019) grown on LB Agar plates with 100ug/mL ampicillin. Plasmids from single clones
511 were isolated via miniprep (Macherey-Nagel 740499) and sequenced to confirm successful
512 cloning.

513

514 Lentivirus Production

515 Lentivirus was produced by transfection of HEK293T cells as adapted from Dull et al. 1998 [101].
516 HEK293T cells were grown in Dulbecco's Modified Eagle Medium (DMEM; Gibco 11965092) with
517 10% bovine calf serum (Cytiva SH30073) at 37 °C in a 5% CO_2 incubator. The day before
518 transfection, ~10^7 cells were plated per 15cm dish coated in 0.1% gelatin. Media was changed
519 just prior to transfection. For one 15cm dish, 22.5ug of transfer vector was combined with 14.7ug
520 of pMDLg/pRRE (Addgene plasmid #12251), 5.7ug of pRSV.Rev (Addgene plasmid #12253), and
521 7.9ug of pMD2.G (Addgene plasmid #12259) in a 15mL conical tube. The plasmid mixture was
522 added to 1mL of 278 uM $CaCl_2$ (Sigma C1016) and mixed thoroughly before adding 1mL of 2x
523 BBS solution [280 mM NaCl (Fisher Scientific S271-1), 50 mM BES (Millipore 391334), 1.5mM
524 Na_2HPO_4 (Sigma S5136); pH = 6.95] dropwise. Tubes were mixed by inversion, incubated at room
525 temperature for 1 min, and then added dropwise to HEK293T dish. Cell culture media was
526 changed after 16-24 h. Conditioned media was then collected every 24 h for 2 days; conditioned

527 media from the same plate was combined over the two collections. Conditioned media was
528 centrifuged at 2000 x g for 10 minutes to pellet debris and filtered through 0.22-um-pore-size PES
529 filter (Millipore SCGP00525). To concentrate virus, filtered media was incubated with PEG 8000
530 (Sigma P2139) and NaCl, at a final concentration of 5% and 0.15M respectively, overnight at 4°C,
531 then centrifuged at 3000 x g for 20 min. The pellet was resuspended in DMEM/F12 with GlutaMAX
532 (Gibco 10565018) to 1% of the original supernatant volume. The concentrated virus was stored
533 in aliquots at -80°C.

534

535 Midbrain Organoid and Astrocyte Differentiation

536 hiPSC-derived astrocytes were extracted from 100-day-old midbrain organoids as described in
537 Sarrafha et al 2021 and Parfitt et al 2024 [81,102]. In short, hiPSCs were cultured in StemFlex medium
538 (Gibco A3349401) at 37 °C in a 5% CO_2 incubator. hiPSCs were seeded into 125-mL spinner
539 flasks (Corning 3152) and allowed to self-aggregate in StemFlex (Gibco A3349401)
540 supplemented with 10 μM Y-27632 (Tocris 1254) and 1% Penicillin-Streptomycin (Gibco
541 15140122). Once aggregates were between 300 μm and 500 μm, differentiation was initiated by
542 dual-SMAD inhibition with 10 μM SB431542 (Stemgent 04-0010), 100nM LDN193189 (Tocris
543 6053), 1x B27 without Vitamin A (Gibco 12587010) and 1x N2 (Gibco 17502048) in DMEM-F12
544 with GlutaMAX (Gibco 10565018). Midbrain patterning was achieved with the addition of 3 μM
545 CHIR99021 (Tocris 4423), 2 μM purmorphamine (Stemcell 72204), and 1 μM SAG (Cayman
546 11914) starting 4 days after neural induction. After patterning, media was changed to DMEM/F12
547 with GlutaMAX, supplemented with 1x N2, 1x B27 without Vitamin A, 20 ng/mL GDNF (Peprotech
548 450-10), 20 ng/mL BDNF (Peprotech 450-02), 200 μM L-ascorbic acid (Fisher Scientific BP351),
549 100 μM dibutyryl cAMP (Biogems 1698950), and 10 μM DAPT (Cayman 13197). After 35 days,
550 organoids were transferred to ultra-low attachment plates (Corning 3516), with about 5 organoids

551 per mL of media and cultured in DMEM/F12 with GlutaMAX supplemented with 1x N2, 1x B27
552 without Vitamin A, 10 ng/mL GDNF, 10 ng/mL BDNF, and 200 μM ascorbic acid.

553 Astrocytes were extracted from midbrain organoids starting at day 100. Organoids were gently
554 dissociated in a trypsin enzyme solution (TrypLE Select, Gibco 12563011) using a glass pipette
555 to break up organoids into large chunks. The organoid chunks from 5-10 organoids were placed
556 on 15cm dishes coated with 0.1% gelatin and maintained in Astrocyte Medium (AM; ScienCell
557 #1801). Astrocytes were allowed to grow out of the organoid chunks until the plate was confluent
558 (about 1 week). At this point, astrocytes can be cryopreserved. Astrocytes were maintained in AM
559 and switched to experimental media [1:1 DMEM/F-12:Neurobasal (Gibco 21103049), 1x B27
560 without Vitamin A, 1x N2, 1x MEM-Non-Essential Amino Acids (Gibco 11140050), 1x GlutaMAX
561 (Gibco 35050061), 10 ng/mL CNTF (Peprotech 450-13)] 2-3 days before imaging.

562

563 Astrocyte Viral Transduction

564 iPSC-derived astrocytes were transduced during regular passaging. In short, astrocytes were
565 lifted, spun down, resuspended in AM media, and divided into 1.5mL microcentrifuge tubes,
566 depending on the desired split ratio and number of transductions. The virus was added to the cell
567 suspension and incubated for 5-10 minutes before plating the mixture. Media was topped off such
568 that the final dilution of the virus in media was 1:50. Depending on the viral titer, this dilution
569 sometimes increased or decreased. Astrocytes can also be transduced without passage by
570 adding the virus directly to the media. Media is changed after 24 hours. Antibiotics were added to
571 the media, if relevant, starting at least 3 days after transduction.

572

573 ## MitoTracker and LysoTracker

574 For MitoTracker staining, astrocytes were incubated with 100 nM of MitoTracker DeepRed
575 (Thermo Scientific M22425) for 30 min at 37 °C. For LysoTracker staining, astrocytes were
576 incubated 100 nM of LysoTracker DeepRed (Thermo Scientific L12492) for 5 min at 37 °C. Cells
577 were then washed twice with PBS before incubation with Hoechst 33342 (Thermo Scientific
578 62249).

579

580 ## qPCR

581 RNA was extracted from samples using TRIzol (Invitrogen 15596018) and an RNA extraction kit
582 following the manufacturer's recommended protocol (Zymo R2062). RNA concentration and purity
583 were measured on a spectrophotometer. cDNA was produced from 1 ug of RNA per sample, using
584 Maxima H Minus Reverse Transcriptase (Thermo Scientific EP0752) and following the
585 manufacturer's recommendations. qPCR reactions were prepared in a 384-well plate (Applied
586 Biosystems 4309849) with 1:10 dilution of cDNA, 2x PowerUp SYBR Green Master Mix (Applied
587 Biosystems A25741) and 1 μM each of forward and reverse primers. qPCRs were run on
588 QuantStudio 7 (Applied Biosystems 4485701) and analyzed using the ΔΔCt method, normalized
589 to *ACTB*. The following primers were used:

590 *ACTB* Forward: CCTGGCACCCAGCACAAT

591 *ACTB* Reverse: GCCGATCCACACGGAGTA

592 *LAMP1* Forward: CAGATGTGTTAGTGGCACCCA

593 *LAMP1* Reverse: TTGGAAAGGTACGCCTGGATG

594

595 # Live Cell Imaging

596 In general, astrocytes were seeded at 10 x 10^3 cells per well of a 96-well plate with a cover glass
597 thickness polystyrene bottom (Greiner 655090) coated in 0.1% gelatin 3-5 days before imaging.
598 Proliferation assays were seeded at 8 x 10^3 cells per well and started 1 day after seeding. Before
599 imaging, cells were incubated with Hoechst 33342 (Thermo Scientific 62249) or DRAQ5 (Thermo
600 Scientific 52251) for 10 minutes.

601 Wide-field live cell imaging was performed using the Thermo Scientific CX7 High Content
602 Screening Platform with 20x and 40x objective lenses (LUCPLFLN20x and LUCPLFLN40x). The
603 microscope was equipped with an incubation unit that maintained temperature, CO_2, and humidity
604 during image acquisition. Confocal images were acquired on a Nikon Ti2E AX R confocal
605 microscope with a 20x objective lens (PLAN APO λD 20x) and 6x optical zoom. Each well was
606 imaged in 5 (confocal) or 25-36 (widefield) different areas, with the average of those images
607 represented as a single data point.

608

609 # ImageJ Image Analysis

610 <u>Nuclear Proliferation:</u> Nuclear proliferation was quantified by converting images to a binary based
611 on a threshold and then using 'Analyze Particles' to obtain a count for the number of nuclei in a
612 field. The same threshold and parameters were kept for all time points.

613 <u>Mitochondrial Fragmentation:</u> Mitochondrial fragmentation was measured using the ImageJ
614 plugin, Mitochondrial Analyzer [103]. For thresholding, the "Block Size" was set to 1.45 microns and
615 the "C-Value" was set to 5.

616 Ratiometric Quantification: Ratiometric quantifications for roGFP2, Timer, and Lemon were
617 achieved by measuring the mean grey value in both channels of interest. The values for each
618 channel were then divided to generate the ratio of relative intensity between the two channels.

619 Kymograph Analysis: Kymograph analysis of mitochondrial movement was achieved using the
620 Image J plugins KymographClear 2.0 and KymographDirect [104]. KymographClear 2.0 was used
621 to trace mitochondrial trajectories and generate kymographs from which stationary and motile
622 mitochondria were identified. KymographDirect was then used to extract quantitative information
623 from the trajectories of the motile mitochondria.

624

625 Cell Profiler Image Analysis [72,105]

626 Subcellular Co-localization: For nuclear co-localization, nuclei in the genetically encoded
627 fluorophore channel and the DRAQ5 channel were identified, and nuclei from cells that were not
628 transduced were filtered out. For lysosomal and mitochondrial co-localization, propagation from
629 the nuclear stain was used to identify cell bodies. Cells were filtered to only analyze those with
630 lentivirus signal within the cell body. Co-localization was reported as the Mander's coefficient
631 indicating the overlap of the genetically encoded fluorophore with the commercially available
632 stain.

633 Lysosomal Distribution: Cells were defined by nuclei and full cell fluorophore signal. Lamp1-
634 mCherry signal was assigned to the cell body with which it overlapped. Only cells that were
635 successfully transduced were included in the analysis. The distribution of the Lamp1-mCherry
636 signal was calculated using the "MeasureObjectIntensityDistribution" with two bins generated for
637 each cell using the nuclei as the center of the cell. Bins were scaled such that the inner bin
638 (perinuclear) was always the same percent of total cell area regardless of cell size.

639

640 ## Quantification and statistical analysis

641 All experiments were conducted with 3-6 replicates. All quantifications were represented as
642 mean ± standard deviation, except for the violin plots of the kymograph analysis. Details on data
643 visualization, sample size, and images per replicate are included in figure captions. Details on
644 statistical tests and significance are included in the text. All statistical tests were conducted in
645 *GraphPad Prism* and graphs were generated in *GraphPad Prism*.

646

647 # Figure Legends

648 **Fig. 1: A toolbox of lentiviral plasmids developed and validated for subcellular localization**
649 **of fluorophores (A)** Schematic of lentiviral plasmids highlighting the combinatorial power of the
650 toolbox components. Generated using BioRender **(B)** Schematic demonstrating the cloning
651 strategies used to generate the constructs used in this study as well as any future constructs.
652 Generated using BioRender **(C)** Representative images of subcellular localization validation with
653 available dyes in hiPSC-derived astrocytes and Mander's co-efficient for overlap of the genetically
654 encoded fluorophore with the dye. Bars represent mean values and error bars represent standard
655 deviation. Top: H2B-mTagBFP2 and DRAQ5 (n = 3; each replicate is an average over 16 images);
656 Middle: LAMP1-mCherry and LysoTracker Deep Red; nuclei stained with Hoechst33342 (n = 4;
657 each replicate is an average over 4 images); Bottom: COX8A-Emerald and MitoTracker Deep
658 Red; nuclei stained with Hoechst33342 (n = 3, each replicate is an average over 36 images).
659 Scale bars = 50 μm **(D)** Representative images of combinatorial applications of GEM-SCOPe.

660 Top: Cell expressing LAMP1-Emerald and COX8A-mCherry. Bottom: cell expression LAMP1-
661 mCherry and COX8A-Emerald. Nuclei were stained with DRAQ5. Scale bars = 50 μm.

662 **Fig. 2: Nucleus-localized fluorophores offer improvements over available stains for**
663 **multiday imaging (A)** Schematic of the lentiviral construct localizing mTagBFP2 to the nucleus
664 with an H2B fusion protein and antibiotic resistance to puromycin used in the following panels **(B)**
665 Representative images of H2B-mTagBFP2 and DRAQ5 nuclear stain 1 hour (top) and 24 hours
666 (bottom) after adding DRAQ5 to the cell cultures. **(C)** Quantification of the percent of stain
667 localized to the nuclear area versus the cytoplasm 1 hour and 24 hours after adding DRAQ5 to
668 cell cultures. The central bar represents the mean and the error bars represent the standard
669 deviation (n = 3 per time point; each replicate is an average over 36 images) **(D)** Schematic of the
670 lentiviral construct localizing Emerald or mCherry to the nucleus with an H2B fusion protein and
671 antibiotic resistance to puromycin used in the following panels **(E)** Representative images of
672 nuclei from *PRKN*$^{+/+}$ astrocytes, labeled with H2B-Emerald, and *PRKN* $^{-/-}$ astrocytes, labeled with
673 H2B-mCherry, cultured together during a proliferation assay. Images were taken 24 hours (top)
674 after seeding and 72 hours (bottom) after seeding **(F)** Quantification of number of *PRKN*$^{+/+}$ and
675 *PRKN*$^{-/-}$ nuclei per image field 24 hours and 72 hours after seeding. Dots represent mean values
676 and error bars represent standard deviation (n = 3 per time point; each replicate is an average
677 over 25 images). Scale bars = 50 μm. All images were acquired on the CX7 HCS platform with a
678 20x objective lens.

679 **Fig. 3: Lysosome-localized fluorophores reveal changes in lysosomal distribution upon**
680 **chemical and genetic perturbation (A)** Schematic of the lentiviral constructs used in the
681 following panels localizing (top) mCherry to the lysosome with the 5' sequence of *LAMP1* and
682 (bottom) Emerald to the whole cell by not including a localization sequence. **(B)** Representative
683 images of astrocytes transduced with Emerald and LAMP1-mCherry lentiviruses and treated with
684 100 nM bafilomycin A1 (bottom) or a vehicle (DMSO; top). Nuclei were stained with

685 Hoechst33342. Far right: Output from CellProfiler showing the distribution Lamp1-mCherry signal
686 as a fraction of signal in each bin. Darker blue indicates a higher fraction of signal in that bin.
687 Scale bars = 50 µm. **(C)** Quantification of lysosomal number per cell (left), average vesicle area
688 (middle) and fraction of perinuclear lysosomes (right) using Lamp1-mCherry signal in vehicle
689 (DMSO) and bafilomycin A1 (100 nM) treated astrocytes. Emerald was used to determine cell
690 boundaries. Central bars represent mean and error bars represent standard deviation (n = 4; each
691 replicate is an average over 10 images). **(D)** Representative images of *PRKN*$^{+/+}$ (top) and *PRKN*$^{-}$
692 $^{/-}$ (bottom) astrocytes transduced with cytoplasmic Emerald and LAMP1-mCherry lentiviruses.
693 Nuclei were stained with Hoechst33342. Far right: Output from CellProfiler showing the
694 distribution Lamp1-mCherry signal as a fraction of signal in each bin. Darker blue indicates a
695 higher fraction of signal in that bin. Scale bars = 25 µm. (**E**) Quantification of Lamp1-mCherry
696 signal in *PRKN*$^{+/+}$ and *PRKN*$^{-/-}$ astrocytes to measure lysosomal number per cell (left), average
697 vesicle area (middle) and fraction of perinuclear lysosomes (right). Emerald fluorescence was
698 used to determine cell boundaries. Central bars represent mean and error bars represent
699 standard deviation (n = 6; each replicate is an average over 7 images). All images were acquired
700 on a Nikon Ti2E AX R confocal microscope with a 20x objective lens and 6x optical zoom.

701 **Fig. 4: Mitochondria-localized fluorophores resolve changes in mitochondrial network**
702 **dynamics (A)** Schematic of the lentiviral construct used in the following panels localizing Emerald
703 to the mitochondria with the targeting sequence of COX8A. **(B)** Representative images of
704 astrocytes transduced with COX8A-Emerald and treated with a vehicle (DMSO; top) or 2 uM
705 oligomycin (bottom). Nuclei were stained with Hoechst33342. High magnification images (far
706 right) highlight the changes to the mitochondrial network upon oligomycin treatment. Scale bars
707 = 50 µm. **(C)** Quantification of mean mitochondrial area, mean mitochondrial branch length, and
708 mean aspect ratio upon oligomycin treatment. Central bars represent mean and error bars
709 represent standard deviation (n = 3; each replicate is an average over 36 images) **(D)**

710 Representative images of mitochondria labeled with COX8A-Emerald moving along *PRKN*$^{-/-}$
711 neuron axons in the anterograde (left) and retrograde (right) directions. Scale bars = 5 μm. Images
712 were taken on a Leica DMi8 microscope for 1 hour per field **(E-F**). Quantification of mitochondrial
713 run length (left) and run time (right) of COX8A-Emerald labeled mitochondria in *PRKN*$^{+/+}$ and
714 *PRKN*$^{-/-}$ dopaminergic neuron axons moving anterograde (E) and retrograde (F) as determined
715 by kymograph analysis (average of n = 37.5 organoids for anterograde and 23.5 organoids for
716 retrograde; each replicate is an average over 1-3 fields).

717 **Fig. 5: Timer fluorophore measures changes in subcellular mitochondrial turnover in**
718 ***PRKN*$^{-/-}$(A)** Schematic demonstrating how the fluorescent protein Timer works. Timer undergoes
719 a fluorescent shift from a green emission to a red emission overtime; analysis of Timer relies on
720 examining the ratio between the red and green emission. **(B)** Schematic of the lentiviral construct
721 used in the following panels localizing Timer to the mitochondria by using the targeting sequence
722 of COX8A. **(C)** Representative images of astrocytes transduced with COX8A-Timer and treated
723 with a vehicle (DMSO; top) or 100 nM bafilomycin A1 (bottom) for 24 hours. Images were acquired
724 with a 488-excitation line and a 594-excitation line. Far right: ratiometric representation of the red
725 channel divided by the green channel and pseudo colored so that orange, yellow and white
726 indicate more relative red emission and black and purple indicate more relative green emission.
727 Nuclei were stained with DRAQ5. Scale bars = 50 μm. **(D)** Quantification of the ratio of mean
728 intensity of emission from excitation with a 594nm laser to the mean intensity of emission from
729 excitation with a 488 nm laser in astrocytes expressing COX8A-Timer and treated with a vehicle
730 (DMSO) or 100 nM bafilomycin A1 for 24 hours. Central bars represent mean and error bars
731 represent standard deviation (n = 6; each replicate is an average over 25 images). (**E**)
732 Representative images of *PRKN*$^{+/+}$ and *PRKN*$^{-/-}$ astrocytes transduced with COX8A-Timer.
733 Images were acquired with a 488-excitation line and a 594-excitation line. Far right: ratiometric
734 representation of the red channel divided by the green channel and pseudo colored so that

735 orange, yellow and white indicate more relative red emission and black and purple indicate more
736 relative green emission. Nuclei were stained with DRAQ5. Scale bars = 50 μm. **(F)** Quantification
737 of the ratio of mean intensity of emission from excitation with a 594nm laser to the mean intensity
738 of emission from excitation with a 488 nm laser in *PRKN*$^{+/+}$ and *PRKN*$^{-/-}$ astrocytes expressing
739 COX8A-Timer. Central bars represent mean and error bars represent standard deviation (n = 3;
740 each replicate is an average over 25 images). **(G)** Quantification of mean intensity normalized by
741 nuclear area of green and red fluorescence in *PRKN*$^{+/+}$ and *PRKN*$^{-/-}$ astrocytes expressing
742 COX8A-Timer. Central bars represent mean and error bars represent standard deviation (n = 3;
743 each replicate is an average over 25 images). All images were acquired on a CX7 HCS platform
744 with a 20x objective lens.

745 **Fig. 6: GRX1-roGFP2 fluorophore is used to quantify glutathione oxidation in chemical and**
746 **genetic models of oxidative stress (A)** Schematic demonstrating how the fluorescent protein
747 fusion Grx1-roGFP2 works. Oxidation of Grx1 upon the oxidation of glutathione results in the
748 eventual oxidation of roGFP2, shifting its emission spectrum from green to blue. **(B)** Schematic
749 of the lentiviral construct used in the following panels localizing Grx1-roGFP2 to the mitochondria.
750 This fluorophore was localized using atp-9 instead of COX8A. **(C)** Representative images of
751 astrocytes transduced with mito-GRX1-roGFP2 and treated with a vehicle (DMSO; top) or 100
752 nM bafilomycin A1 (bottom) for 24 hours. Images were acquired with a 405-excitation laser and a
753 488-excitation laser. Far right: ratiometric representation of the green channel divided by the blue
754 channel and then pseudo colored so that orange, yellow and white indicate more relative green
755 emission while black and purple represent more blue emission. Nuclei were stained with DRAQ5.
756 Scale bars = 50 μm. **(D)** Quantification of the ratio of mean intensity from 488-excitation to the
757 mean intensity from 405 excitation. In astrocytes expression mito-Grx1-roGFP2 and treated with
758 a vehicle or 100 nM bafilomycin A1. Central bars represent mean and error bars represent
759 standard deviation (n = 6; each replicate is an average over 25 images). **(E)** Quantification of

760 mean intensity normalized by nuclear area of blue and green fluorescence in vehicle and
761 bafilomycin A1 treated astrocytes expressing mito-Grx1-roGFP2. Central bars represent mean
762 and error bars represent standard deviation (n = 6; each replicate is an average of 25 images).
763 **(F)** Representative images of *PRKN*$^{+/+}$ and *PRKN*$^{-/-}$ astrocytes transduced with mito-Grx1-
764 roGFP2. Images were acquired with a 405-excitation laser and a 588-excitation laser. Far right:
765 ratiometric representation of the green channel divided by the blue channel and pseudo colored
766 so that orange, yellow and white indicate more relative green emission and black and purple
767 indicate more relative blue emission. Nuclei were stained with DRAQ5. Scale bars = 50 μm. **(G)**
768 Quantification of the ratio of mean intensity of emission from excitation with a 488nm laser to the
769 mean intensity of emission from excitation with a 405 nm laser in *PRKN*$^{+/+}$ and *PRKN*$^{-/-}$ astrocytes
770 expressing mito-Grx1-roGFP2. Central bars represent mean and error bars represent standard
771 deviation (n = 3; each replicate is an average over 16 images).

772

773

774 # References

775 1. Willis, A.W., Roberts, E., Beck, J.C., Fiske, B., Ross, W., Savica, R., Van Den Eeden,
776 S.K., Tanner, C.M., Marras, C., and Parkinson's Foundation, P.G. (2022). Incidence of
777 Parkinson disease in North America. NPJ Parkinsons Dis *8*, 170. 10.1038/s41531-022-
778 00410-y.
779 2. Vazquez-Velez, G.E., and Zoghbi, H.Y. (2021). Parkinson's Disease Genetics and
780 Pathophysiology. Annu Rev Neurosci *44*, 87-108. 10.1146/annurev-neuro-100720-
781 034518.

3. Schneider, S.A., and Obeso, J.A. (2015). Clinical and pathological features of Parkinson's disease. Curr Top Behav Neurosci *22*, 205-220. 10.1007/7854_2014_317.

4. Varadi, C. (2020). Clinical Features of Parkinson's Disease: The Evolution of Critical Symptoms. Biology (Basel) *9*. 10.3390/biology9050103.

5. Jankovic, J. (2008). Parkinson's disease: clinical features and diagnosis. J Neurol Neurosurg Psychiatry *79*, 368-376. 10.1136/jnnp.2007.131045.

6. Naoi, M., and Maruyama, W. (1999). Cell death of dopamine neurons in aging and Parkinson's disease. Mech Ageing Dev *111*, 175-188. 10.1016/s0047-6374(99)00064-0.

7. Spillantini, M.G., Schmidt, M.L., Lee, V.M., Trojanowski, J.Q., Jakes, R., and Goedert, M. (1997). Alpha-synuclein in Lewy bodies. Nature *388*, 839-840. 10.1038/42166.

8. Ohama, E., and Ikuta, F. (1976). Parkinson's disease: distribution of Lewy bodies and monoamine neuron system. Acta Neuropathol *34*, 311-319. 10.1007/BF00696560.

9. Hartmann, A. (2004). Postmortem studies in Parkinson's disease. Dialogues Clin Neurosci *6*, 281-293. 10.31887/DCNS.2004.6.3/ahartmann.

10. Helmchen, F., Fee, M.S., Tank, D.W., and Denk, W. (2001). A miniature head-mounted two-photon microscope. high-resolution brain imaging in freely moving animals. Neuron *31*, 903-912. 10.1016/s0896-6273(01)00421-4.

11. Zong, W., Wu, R., Li, M., Hu, Y., Li, Y., Li, J., Rong, H., Wu, H., Xu, Y., Lu, Y., et al. (2017). Fast high-resolution miniature two-photon microscopy for brain imaging in freely behaving mice. Nat Methods *14*, 713-719. 10.1038/nmeth.4305.

12. Chen, K., Tian, Z., and Kong, L. (2022). Advances of optical miniscopes for in vivo imaging of neural activity in freely moving animals. Front Neurosci *16*, 994079. 10.3389/fnins.2022.994079.

13. Potashkin, J.A., Blume, S.R., and Runkle, N.K. (2010). Limitations of animal models of Parkinson's disease. Parkinsons Dis *2011*, 658083. 10.4061/2011/658083.

807 14. Chia, S.J., Tan, E.K., and Chao, Y.X. (2020). Historical Perspective: Models of
808 Parkinson's Disease. Int J Mol Sci *21*. 10.3390/ijms21072464.
809 15. Ahfeldt, T., Ordureau, A., Bell, C., Sarrafha, L., Sun, C., Piccinotti, S., Grass, T., Parfitt,
810 G.M., Paulo, J.A., Yanagawa, F., et al. (2020). Pathogenic Pathways in Early-Onset
811 Autosomal Recessive Parkinson's Disease Discovered Using Isogenic Human
812 Dopaminergic Neurons. Stem Cell Reports *14*, 75-90. 10.1016/j.stemcr.2019.12.005.
813 16. Raja, W.K., Neves, E., Burke, C., Jiang, X., Xu, P., Rhodes, K.J., Khurana, V.,
814 Scannevin, R.H., and Chung, C.Y. (2022). Patient-derived three-dimensional cortical
815 neurospheres to model Parkinson's disease. PLoS One *17*, e0277532.
816 10.1371/journal.pone.0277532.
817 17. Chlebanowska, P., Tejchman, A., Sulkowski, M., Skrzypek, K., and Majka, M. (2020).
818 Use of 3D Organoids as a Model to Study Idiopathic Form of Parkinson's Disease. Int J
819 Mol Sci *21*. 10.3390/ijms21030694.
820 18. Kim, H., Park, H.J., Choi, H., Chang, Y., Park, H., Shin, J., Kim, J., Lengner, C.J., Lee,
821 Y.K., and Kim, J. (2019). Modeling G2019S-LRRK2 Sporadic Parkinson's Disease in 3D
822 Midbrain Organoids. Stem Cell Reports *12*, 518-531. 10.1016/j.stemcr.2019.01.020.
823 19. Shimomura, O., Johnson, F.H., and Saiga, Y. (1962). Extraction, purification and
824 properties of aequorin, a bioluminescent protein from the luminous hydromedusan,
825 Aequorea. J Cell Comp Physiol *59*, 223-239. 10.1002/jcp.1030590302.
826 20. Wang, M., Da, Y., and Tian, Y. (2023). Fluorescent proteins and genetically encoded
827 biosensors. Chem Soc Rev *52*, 1189-1214. 10.1039/d2cs00419d.
828 21. Ovechkina, V.S., Zakian, S.M., Medvedev, S.P., and Valetdinova, K.R. (2021).
829 Genetically Encoded Fluorescent Biosensors for Biomedical Applications. Biomedicines
830 *9*. 10.3390/biomedicines9111528.

831 22. Terskikh, A., Fradkov, A., Ermakova, G., Zaraisky, A., Tan, P., Kajava, A.V., Zhao, X.,
832 Lukyanov, S., Matz, M., Kim, S., et al. (2000). "Fluorescent timer": protein that changes
833 color with time. Science *290*, 1585-1588. 10.1126/science.290.5496.1585.
834 23. Nakai, J., Ohkura, M., and Imoto, K. (2001). A high signal-to-noise Ca(2+) probe
835 composed of a single green fluorescent protein. Nat Biotechnol *19*, 137-141.
836 10.1038/84397.
837 24. Burgstaller, S., Bischof, H., Gensch, T., Stryeck, S., Gottschalk, B., Ramadani-Muja, J.,
838 Eroglu, E., Rost, R., Balfanz, S., Baumann, A., et al. (2019). pH-Lemon, a Fluorescent
839 Protein-Based pH Reporter for Acidic Compartments. ACS Sens *4*, 883-891.
840 10.1021/acssensors.8b01599.
841 25. Gutscher, M., Pauleau, A.L., Marty, L., Brach, T., Wabnitz, G.H., Samstag, Y., Meyer,
842 A.J., and Dick, T.P. (2008). Real-time imaging of the intracellular glutathione redox
843 potential. Nat Methods *5*, 553-559. 10.1038/nmeth.1212.
844 26. Nalls, M.A., Blauwendraat, C., Vallerga, C.L., Heilbron, K., Bandres-Ciga, S., Chang, D.,
845 Tan, M., Kia, D.A., Noyce, A.J., Xue, A., et al. (2019). Identification of novel risk loci,
846 causal insights, and heritable risk for Parkinson's disease: a meta-analysis of genome-
847 wide association studies. Lancet Neurol *18*, 1091-1102. 10.1016/S1474-4422(19)30320-
848 5.
849 27. Karimi-Moghadam, A., Charsouei, S., Bell, B., and Jabalameli, M.R. (2018). Parkinson
850 Disease from Mendelian Forms to Genetic Susceptibility: New Molecular Insights into
851 the Neurodegeneration Process. Cell Mol Neurobiol *38*, 1153-1178. 10.1007/s10571-
852 018-0587-4.
853 28. Jia, F., Fellner, A., and Kumar, K.R. (2022). Monogenic Parkinson's Disease: Genotype,
854 Phenotype, Pathophysiology, and Genetic Testing. Genes (Basel) *13*.
855 10.3390/genes13030471.

856 29. Guadagnolo, D., Piane, M., Torrisi, M.R., Pizzuti, A., and Petrucci, S. (2021). Genotype-
857 Phenotype Correlations in Monogenic Parkinson Disease: A Review on Clinical and
858 Molecular Findings. Front Neurol *12*, 648588. 10.3389/fneur.2021.648588.
859 30. Lesage, S., Lunati, A., Houot, M., Romdhan, S.B., Clot, F., Tesson, C., Mangone, G.,
860 Toullec, B.L., Courtin, T., Larcher, K., et al. (2020). Characterization of Recessive
861 Parkinson Disease in a Large Multicenter Study. Ann Neurol *88*, 843-850.
862 10.1002/ana.25787.
863 31. Pickrell, A.M., and Youle, R.J. (2015). The roles of PINK1, parkin, and mitochondrial
864 fidelity in Parkinson's disease. Neuron *85*, 257-273. 10.1016/j.neuron.2014.12.007.
865 32. Tanaka, K. (2020). The PINK1-Parkin axis: An Overview. Neurosci Res *159*, 9-15.
866 10.1016/j.neures.2020.01.006.
867 33. Kamienieva, I., Duszynski, J., and Szczepanowska, J. (2021). Multitasking guardian of
868 mitochondrial quality: Parkin function and Parkinson's disease. Transl Neurodegener *10*,
869 5. 10.1186/s40035-020-00229-8.
870 34. Lois, C., Hong, E.J., Pease, S., Brown, E.J., and Baltimore, D. (2002). Germline
871 transmission and tissue-specific expression of transgenes delivered by lentiviral vectors.
872 Science *295*, 868-872. 10.1126/science.1067081.
873 35. Schorpp, M., Jäger, R., Schellander, K., Schenkel, J., Wagner, E.F., Weiher, H., and
874 Angel, P. (1996/05/01). The Human Ubiquitin C Promoter Directs High Ubiquitous
875 Expression of Transgenes in Mice. Nucleic Acids Research *24*. 10.1093/nar/24.9.1787.
876 36. Zufferey, R., Donello, J.E., Trono, D., and Hope, T.J. (1999/04). Woodchuck Hepatitis
877 Virus Posttranscriptional Regulatory Element Enhances Expression of Transgenes
878 Delivered by Retroviral Vectors. Journal of Virology *73*. 10.1128/jvi.73.4.2886-
879 2892.1999.
880 37. Higashimoto, T., Urbinati, F., Perumbeti, A., Jiang, G., Zarzuela, A., Chang, L.J., Kohn,
881 D.B., and Malik, P. (2007). The woodchuck hepatitis virus post-transcriptional regulatory

882 element reduces readthrough transcription from retroviral vectors. Gene Therapy *14*,
883 1298-1304. 10.1038/sj.gt.3302979.
884 38. Mosammaparast, N., Jackson, K.R., Guo, Y., Brame, C.J., Shabanowitz, J., Hunt, D.F.,
885 and Pemberton, L.F. (2001). Nuclear import of histone H2A and H2B is mediated by a
886 network of karyopherins. J Cell Biol *153*, 251-262. 10.1083/jcb.153.2.251.
887 39. Marino-Ramirez, L., Kann, M.G., Shoemaker, B.A., and Landsman, D. (2005). Histone
888 structure and nucleosome stability. Expert Rev Proteomics *2*, 719-729.
889 10.1586/14789450.2.5.719.
890 40. Smith, P.J., Wiltshire, M., and Errington, R.J. (2004). DRAQ5 labeling of nuclear DNA in
891 live and fixed cells. Curr Protoc Cytom *Chapter 7*, Unit 7 25.
892 10.1002/0471142956.cy0725s28.
893 41. Zhitomirsky, B., Farber, H., and Assaraf, Y.G. (2018). LysoTracker and MitoTracker Red
894 are transport substrates of P-glycoprotein: implications for anticancer drug design
895 evading multidrug resistance. J Cell Mol Med *22*, 2131-2141. 10.1111/jcmm.13485.
896 42. Chazotte, B. (2011). Labeling lysosomes in live cells with LysoTracker. Cold Spring Harb
897 Protoc *2011*, pdb prot5571. 10.1101/pdb.prot5571.
898 43. Dang, Q., Zhou, H., Qian, J., Yang, L., Huang, J., Zhang, Y., and Shi, W. (2018). LAMP1
899 Overexpression Predicts for Poor Prognosis in Diffuse Large B-cell Lymphoma. Clin
900 Lymphoma Myeloma Leuk *18*, 749-754. 10.1016/j.clml.2018.07.288.
901 44. Wang, Q.Q., Yao, J., Jin, Q., Wang, X.D., Zhu, H.J., Huang, F., Wang, W., Qiang, J.F.,
902 and Ni, Q.C. (2017). LAMP1 expression is associated with poor prognosis in breast
903 cancer. Oncol Lett *14*, 4729-4735. 10.3892/ol.2017.6757.
904 45. Xu, Y., Cao, X., Zhang, S., Zhang, Y., and Shen, Z. (2017). High expression of LAMP1
905 as a prognostic marker in patients with epithelial ovarian cancer. Int J Clin Exp Pathol
906 *10*, 9104-9111.

907 46. Ranjbar, M.A., and Jamshidi, M. (2022). Overexpression of Lysosome-Associated
908 Membrane Protein 1 in Oral Squamous Cell Carcinoma and its Correlation with Tumor
909 Differentiation and Metastasis. Iran J Otorhinolaryngol *34*, 3-8.
910 10.22038/IJORL.2021.51683.2772.
911 47. Zong, S., Wu, M., Gu, J., Liu, T., Guo, R., and Yang, M. (2018). Structure of the intact
912 14-subunit human cytochrome c oxidase. Cell Res *28*, 1026-1034. 10.1038/s41422-018-
913 0071-1.
914 48. Cunatova, K., Reguera, D.P., Houstek, J., Mracek, T., and Pecina, P. (2020). Role of
915 cytochrome c oxidase nuclear-encoded subunits in health and disease. Physiol Res *69*,
916 947-965. 10.33549/physiolres.934446.
917 49. Partikian, A., Olveczky, B., Swaminathan, R., Li, Y., and Verkman, A.S. (1998). Rapid
918 diffusion of green fluorescent protein in the mitochondrial matrix. J Cell Biol *140*, 821-
919 829. 10.1083/jcb.140.4.821.
920 50. Hoogewijs, K., James, A.M., Smith, R.A., Gait, M.J., Murphy, M.P., and Lightowlers, R.N.
921 (2016). Assessing the Delivery of Molecules to the Mitochondrial Matrix Using Click
922 Chemistry. Chembiochem *17*, 1312-1316. 10.1002/cbic.201600188.
923 51. Candas, D., Qin, L., Fan, M., and Li, J.J. (2016). Experimental Approaches to Study
924 Mitochondrial Localization and Function of a Nuclear Cell Cycle Kinase, Cdk1. J Vis Exp,
925 53417. 10.3791/53417.
926 52. Chazotte, B. (2011). Labeling mitochondria with MitoTracker dyes. Cold Spring Harb
927 Protoc *2011*, 990-992. 10.1101/pdb.prot5648.
928 53. Durand, R.E., and Olive, P.L. (1982). Cytotoxicity, Mutagenicity and DNA damage by
929 Hoechst 33342. J Histochem Cytochem *30*, 111-116. 10.1177/30.2.7061816.
930 54. Wiezorek, C. (1984). Cell cycle dependence of Hoechst 33342 dye cytotoxicity on sorted
931 living cells. Histochemistry *81*, 493-495. 10.1007/BF00489756.

932 55. Solano, R.M., Casarejos, M.J., Menendez-Cuervo, J., Rodriguez-Navarro, J.A., Garcia
933 de Yebenes, J., and Mena, M.A. (2008). Glial dysfunction in parkin null mice: effects of
934 aging. J Neurosci *28*, 598-611. 10.1523/JNEUROSCI.4609-07.2008.
935 56. Rouland, L., Duplan, E., Ramos Dos Santos, L., Bernardin, A., Katula, K.S., Manfioletti,
936 G., Idbaih, A., Checler, F., and Alves da Costa, C. (2021). Therapeutic potential of parkin
937 as a tumor suppressor via transcriptional control of cyclins in glioblastoma cell and
938 animal models. Theranostics *11*, 10047-10063. 10.7150/thno.57549.
939 57. Wahabi, K., Perwez, A., and Rizvi, M.A. (2018). Parkin in Parkinson's Disease and
940 Cancer: a Double-Edged Sword. Mol Neurobiol *55*, 6788-6800. 10.1007/s12035-018-
941 0879-1.
942 58. Yeo, C.W., Ng, F.S., Chai, C., Tan, J.M., Koh, G.R., Chong, Y.K., Koh, L.W., Foong, C.S.,
943 Sandanaraj, E., Holbrook, J.D., et al. (2012). Parkin pathway activation mitigates glioma
944 cell proliferation and predicts patient survival. Cancer Res *72*, 2543-2553. 10.1158/0008-
945 5472.CAN-11-3060.
946 59. Tay, S.P., Yeo, C.W., Chai, C., Chua, P.J., Tan, H.M., Ang, A.X., Yip, D.L., Sung, J.X.,
947 Tan, P.H., Bay, B.H., et al. (2010). Parkin enhances the expression of cyclin-dependent
948 kinase 6 and negatively regulates the proliferation of breast cancer cells. J Biol Chem
949 *285*, 29231-29238. 10.1074/jbc.M110.108241.
950 60. Gong, Y., Zack, T.I., Morris, L.G., Lin, K., Hukkelhoven, E., Raheja, R., Tan, I.L., Turcan,
951 S., Veeriah, S., Meng, S., et al. (2014). Pan-cancer genetic analysis identifies PARK2 as
952 a master regulator of G1/S cyclins. Nat Genet *46*, 588-594. 10.1038/ng.2981.
953 61. Veeriah, S., Taylor, B.S., Meng, S., Fang, F., Yilmaz, E., Vivanco, I., Janakiraman, M.,
954 Schultz, N., Hanrahan, A.J., Pao, W., et al. (2010). Somatic mutations of the Parkinson's
955 disease-associated gene PARK2 in glioblastoma and other human malignancies. Nat
956 Genet *42*, 77-82. 10.1038/ng.491.

957 62. Frade, J.M., and Ovejero-Benito, M.C. (2015). Neuronal cell cycle: the neuron itself and
958 its circumstances. Cell Cycle *14*, 712-720. 10.1080/15384101.2015.1004937.
959 63. Kruman, II, Wersto, R.P., Cardozo-Pelaez, F., Smilenov, L., Chan, S.L., Chrest, F.J.,
960 Emokpae, R., Jr., Gorospe, M., and Mattson, M.P. (2004). Cell cycle activation linked to
961 neuronal cell death initiated by DNA damage. Neuron *41*, 549-561. 10.1016/s0896-
962 6273(04)00017-0.
963 64. Gupta, R., Jha, A., Ambasta, R.K., and Kumar, P. (2021). Regulatory mechanism of
964 cyclins and cyclin-dependent kinases in post-mitotic neuronal cell division. Life Sci *285*,
965 120006. 10.1016/j.lfs.2021.120006.
966 65. Gan-Or, Z., Dion, P.A., and Rouleau, G.A. (2015). Genetic perspective on the role of the
967 autophagy-lysosome pathway in Parkinson disease. Autophagy *11*, 1443-1457.
968 10.1080/15548627.2015.1067364.
969 66. Navarro-Romero, A., Montpeyo, M., and Martinez-Vicente, M. (2020). The Emerging
970 Role of the Lysosome in Parkinson's Disease. Cells *9*. 10.3390/cells9112399.
971 67. Hopfner, F., Mueller, S.H., Szymczak, S., Junge, O., Tittmann, L., May, S., Lohmann, K.,
972 Grallert, H., Lieb, W., Strauch, K., et al. (2020). Rare Variants in Specific Lysosomal
973 Genes Are Associated With Parkinson's Disease. Mov Disord *35*, 1245-1248.
974 10.1002/mds.28037.
975 68. Dehay, B., Martinez-Vicente, M., Caldwell, G.A., Caldwell, K.A., Yue, Z., Cookson, M.R.,
976 Klein, C., Vila, M., and Bezard, E. (2013). Lysosomal impairment in Parkinson's disease.
977 Mov Disord *28*, 725-732. 10.1002/mds.25462.
978 69. Klein, A.D., and Mazzulli, J.R. (2018). Is Parkinson's disease a lysosomal disorder?
979 Brain *141*, 2255-2262. 10.1093/brain/awy147.
980 70. Yoshimori, T., Yamamoto, A., Moriyama, Y., Futai, M., and Tashiro, Y. (1991). Bafilomycin
981 A1, a specific inhibitor of vacuolar-type H(+)-ATPase, inhibits acidification and protein
982 degradation in lysosomes of cultured cells. J Biol Chem *266*, 17707-17712.

983 71. Mauvezin, C., and Neufeld, T.P. (2015). Bafilomycin A1 disrupts autophagic flux by
984 inhibiting both V-ATPase-dependent acidification and Ca-P60A/SERCA-dependent
985 autophagosome-lysosome fusion. Autophagy *11*, 1437-1438.
986 10.1080/15548627.2015.1066957.
987 72. Carpenter, A.E., Jones, T.R., Lamprecht, M.R., Clarke, C., Kang, I.H., Friman, O.,
988 Guertin, D.A., Chang, J.H., Lindquist, R.A., Moffat, J., et al. (2006). CellProfiler: image
989 analysis software for identifying and quantifying cell phenotypes. Genome Biol *7*, R100.
990 10.1186/gb-2006-7-10-r100.
991 73. Johnson, D.E., Ostrowski, P., Jaumouille, V., and Grinstein, S. (2016). The position of
992 lysosomes within the cell determines their luminal pH. J Cell Biol *212*, 677-692.
993 10.1083/jcb.201507112.
994 74. Heuser, J. (1989). Changes in lysosome shape and distribution correlated with changes
995 in cytoplasmic pH. J Cell Biol *108*, 855-864. 10.1083/jcb.108.3.855.
996 75. Parton, R.G., Dotti, C.G., Bacallao, R., Kurtz, I., Simons, K., and Prydz, K. (1991). pH-
997 induced microtubule-dependent redistribution of late endosomes in neuronal and
998 epithelial cells. J Cell Biol *113*, 261-274. 10.1083/jcb.113.2.261.
999 76. Pu, J., Guardia, C.M., Keren-Kaplan, T., and Bonifacino, J.S. (2016). Mechanisms and
1000 functions of lysosome positioning. J Cell Sci *129*, 4329-4339. 10.1242/jcs.196287.
1001 77. Song, P., Trajkovic, K., Tsunemi, T., and Krainc, D. (2016). Parkin Modulates Endosomal
1002 Organization and Function of the Endo-Lysosomal Pathway. J Neurosci *36*, 2425-2437.
1003 10.1523/JNEUROSCI.2569-15.2016.
1004 78. Okarmus, J., Bogetofte, H., Schmidt, S.I., Ryding, M., Garcia-Lopez, S., Ryan, B.J.,
1005 Martinez-Serrano, A., Hyttel, P., and Meyer, M. (2020). Lysosomal perturbations in
1006 human dopaminergic neurons derived from induced pluripotent stem cells with PARK2
1007 mutation. Sci Rep *10*, 10278. 10.1038/s41598-020-67091-6.

1008 79. Twig, G., Elorza, A., Molina, A.J., Mohamed, H., Wikstrom, J.D., Walzer, G., Stiles, L.,
1009 Haigh, S.E., Katz, S., Las, G., et al. (2008). Fission and selective fusion govern
1010 mitochondrial segregation and elimination by autophagy. EMBO J *27*, 433-446.
1011 10.1038/sj.emboj.7601963.
1012 80. Chen, H., Chomyn, A., and Chan, D.C. (2005). Disruption of fusion results in
1013 mitochondrial heterogeneity and dysfunction. J Biol Chem *280*, 26185-26192.
1014 10.1074/jbc.M503062200.
1015 81. Sarrafha, L., Parfitt, G.M., Reyes, R., Goldman, C., Coccia, E., Kareva, T., and Ahfeldt, T.
1016 (2021). High-throughput generation of midbrain dopaminergic neuron organoids from
1017 reporter human pluripotent stem cells. STAR Protoc *2*, 100463.
1018 10.1016/j.xpro.2021.100463.
1019 82. Wang, X., Winter, D., Ashrafi, G., Schlehe, J., Wong, Y.L., Selkoe, D., Rice, S., Steen, J.,
1020 LaVoie, M.J., and Schwarz, T.L. (2011). PINK1 and Parkin target Miro for
1021 phosphorylation and degradation to arrest mitochondrial motility. Cell *147*, 893-906.
1022 10.1016/j.cell.2011.10.018.
1023 83. Hernandez, G., Thornton, C., Stotland, A., Lui, D., Sin, J., Ramil, J., Magee, N., Andres,
1024 A., Quarato, G., Carreira, R.S., et al. (2013). MitoTimer: a novel tool for monitoring
1025 mitochondrial turnover. Autophagy *9*, 1852-1861. 10.4161/auto.26501.
1026 84. Laker, R.C., Xu, P., Ryall, K.A., Sujkowski, A., Kenwood, B.M., Chain, K.H., Zhang, M.,
1027 Royal, M.A., Hoehn, K.L., Driscoll, M., et al. (2014). A novel MitoTimer reporter gene for
1028 mitochondrial content, structure, stress, and damage in vivo. J Biol Chem *289*, 12005-
1029 12015. 10.1074/jbc.M113.530527.
1030 85. Hanson, G.T., Aggeler, R., Oglesbee, D., Cannon, M., Capaldi, R.A., Tsien, R.Y., and
1031 Remington, S.J. (2004). Investigating mitochondrial redox potential with redox-sensitive
1032 green fluorescent protein indicators. J Biol Chem *279*, 13044-13053.
1033 10.1074/jbc.M312846200.

1034 86. Yokomakura, A., Hong, J., Ohuchi, K., Oh, S.E., Lee, J.Y., Mano, N., Takahashi, T.,
1035 Hwang, G.W., and Naganuma, A. (2012). Increased production of reactive oxygen
1036 species by the vacuolar-type (H(+))-ATPase inhibitors bafilomycin A1 and concanamycin
1037 A in RAW 264 cells. J Toxicol Sci *37*, 1045-1048. 10.2131/jts.37.1045.
1038 87. Palacino, J.J., Sagi, D., Goldberg, M.S., Krauss, S., Motz, C., Wacker, M., Klose, J., and
1039 Shen, J. (2004). Mitochondrial dysfunction and oxidative damage in parkin-deficient
1040 mice. J Biol Chem *279*, 18614-18622. 10.1074/jbc.M401135200.
1041 88. Cornejo-Olivas, M.R., Torres, L., Mata, I.F., Mazzetti, P., Rivas, D., Cosentino, C., Inca-
1042 Martinez, M., Cuba, J.M., Zabetian, C.P., and Leverenz, J.B. (2015). A Peruvian family
1043 with a novel PARK2 mutation: Clinical and pathological characteristics. Parkinsonism
1044 Relat Disord *21*, 444-448. 10.1016/j.parkreldis.2015.01.005.
1045 89. Orimo, S., Amino, T., Yokochi, M., Kojo, T., Uchihara, T., Takahashi, A., Wakabayashi, K.,
1046 Takahashi, H., Hattori, N., and Mizuno, Y. (2005). Preserved cardiac sympathetic nerve
1047 accounts for normal cardiac uptake of MIBG in PARK2. Mov Disord *20*, 1350-1353.
1048 10.1002/mds.20594.
1049 90. Gouider-Khouja, N., Larnaout, A., Amouri, R., Sfar, S., Belal, S., Ben Hamida, C., Ben
1050 Hamida, M., Hattori, N., Mizuno, Y., and Hentati, F. (2003). Autosomal recessive
1051 parkinsonism linked to parkin gene in a Tunisian family. Clinical, genetic and pathological
1052 study. Parkinsonism Relat Disord *9*, 247-251. 10.1016/s1353-8020(03)00016-6.
1053 91. Hayashi, S., Wakabayashi, K., Ishikawa, A., Nagai, H., Saito, M., Maruyama, M.,
1054 Takahashi, T., Ozawa, T., Tsuji, S., and Takahashi, H. (2000). An autopsy case of
1055 autosomal-recessive juvenile parkinsonism with a homozygous exon 4 deletion in the
1056 parkin gene. Mov Disord *15*, 884-888. 10.1002/1531-8257(200009)15:5<884::aid-
1057 mds1019>3.0.co;2-8.
1058 92. Schmidt, S., Linnartz, B., Mendritzki, S., Sczepan, T., Lubbert, M., Stichel, C.C., and
1059 Lubbert, H. (2011). Genetic mouse models for Parkinson's disease display severe

1060 pathology in glial cell mitochondria. Hum Mol Genet *20*, 1197-1211.
1061 10.1093/hmg/ddq564.
1062 93. Gerasimova, T., Stepanenko, E., Novosadova, L., Arsenyeva, E., Shimchenko, D.,
1063 Tarantul, V., Grivennikov, I., Nenasheva, V., and Novosadova, E. (2023). Glial Cultures
1064 Differentiated from iPSCs of Patients with PARK2-Associated Parkinson's Disease
1065 Demonstrate a Pro-Inflammatory Shift and Reduced Response to TNFalpha Stimulation.
1066 Int J Mol Sci *24*. 10.3390/ijms24032000.
1067 94. Hastie, E., Cataldi, M., Marriott, I., and Grdzelishvili, V.Z. (2013). Understanding and
1068 altering cell tropism of vesicular stomatitis virus. Virus Res *176*, 16-32.
1069 10.1016/j.virusres.2013.06.003.
1070 95. Sweeney, N.P., and Vink, C.A. (2021). The impact of lentiviral vector genome size and
1071 producer cell genomic to gag-pol mRNA ratios on packaging efficiency and titre. Mol
1072 Ther Methods Clin Dev *21*, 574-584. 10.1016/j.omtm.2021.04.007.
1073 96. Desfarges, S., and Ciuffi, A. (2010). Retroviral integration site selection. Viruses *2*, 111-
1074 130. 10.3390/v2010111.
1075 97. Bonam, S.R., Wang, F., and Muller, S. (2019). Lysosomes as a therapeutic target. Nat
1076 Rev Drug Discov *18*, 923-948. 10.1038/s41573-019-0036-1.
1077 98. Zhang, Z., Yue, P., Lu, T., Wang, Y., Wei, Y., and Wei, X. (2021). Role of lysosomes in
1078 physiological activities, diseases, and therapy. J Hematol Oncol *14*, 79. 10.1186/s13045-
1079 021-01087-1.
1080 99. Javadov, S., Kozlov, A.V., and Camara, A.K.S. (2020). Mitochondria in Health and
1081 Diseases. Cells *9*. 10.3390/cells9051177.
1082 100. Chen, W., Zhao, H., and Li, Y. (2023). Mitochondrial dynamics in health and disease:
1083 mechanisms and potential targets. Signal Transduct Target Ther *8*, 333.
1084 10.1038/s41392-023-01547-9.

1085 101. Dull, T., Zufferey, R., Kelly, M., Mandel, R.J., Nguyen, M., Trono, D., and Naldini, L.
1086 (1998). A third-generation lentivirus vector with a conditional packaging system. J Virol
1087 *72*, 8463-8471. 10.1128/JVI.72.11.8463-8471.1998.
1088 102. Morrone Parfitt, G., Coccia, E., Goldman, C., Whitney, K., Reyes, R., Sarrafha, L., Nam,
1089 K.H., Sohail, S., Jones, D.R., Crary, J.F., et al. (2024). Disruption of lysosomal
1090 proteolysis in astrocytes facilitates midbrain organoid proteostasis failure in an early-
1091 onset Parkinson's disease model. Nat Commun *15*, 447. 10.1038/s41467-024-44732-2.
1092 103. Chaudhry, A., Shi, R., and Luciani, D.S. (2020). A pipeline for multidimensional confocal
1093 analysis of mitochondrial morphology, function, and dynamics in pancreatic beta-cells.
1094 Am J Physiol Endocrinol Metab *318*, E87-E101. 10.1152/ajpendo.00457.2019.
1095 104. Mangeol, P., Prevo, B., and Peterman, E.J. (2016). KymographClear and
1096 KymographDirect: two tools for the automated quantitative analysis of molecular and
1097 cellular dynamics using kymographs. Mol Biol Cell *27*, 1948-1957. 10.1091/mbc.E15-06-
1098 0404.
1099 105. Stirling, D.R., Swain-Bowden, M.J., Lucas, A.M., Carpenter, A.E., Cimini, B.A., and
1100 Goodman, A. (2021). CellProfiler 4: improvements in speed, utility and usability. BMC
1101 Bioinformatics *22*, 433. 10.1186/s12859-021-04344-9.

1102

Figure 1

A.

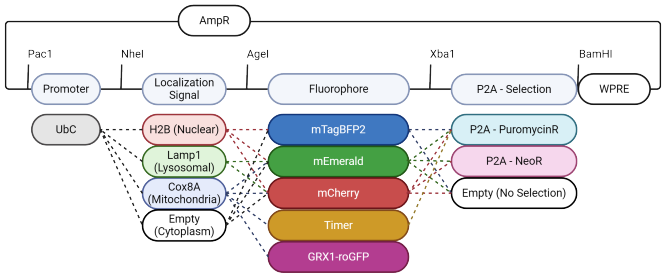

B.

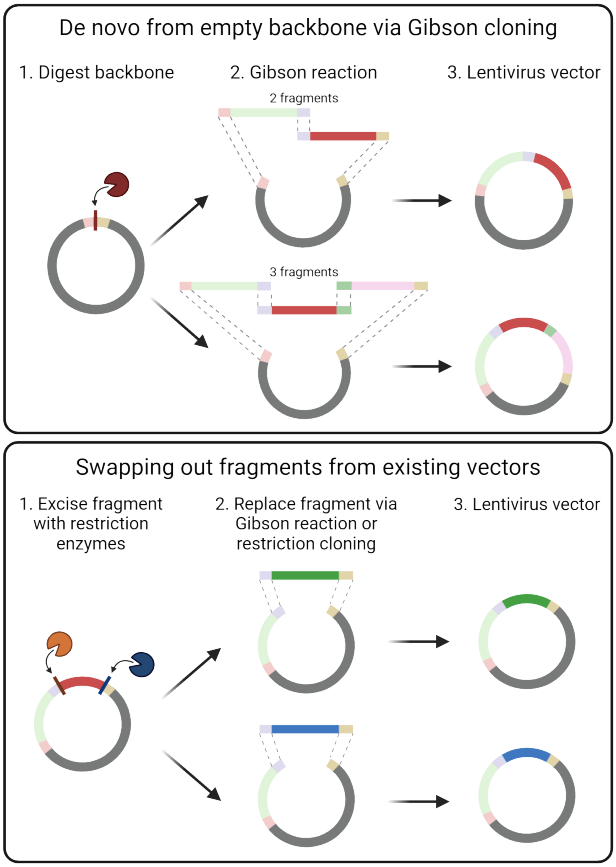

C.

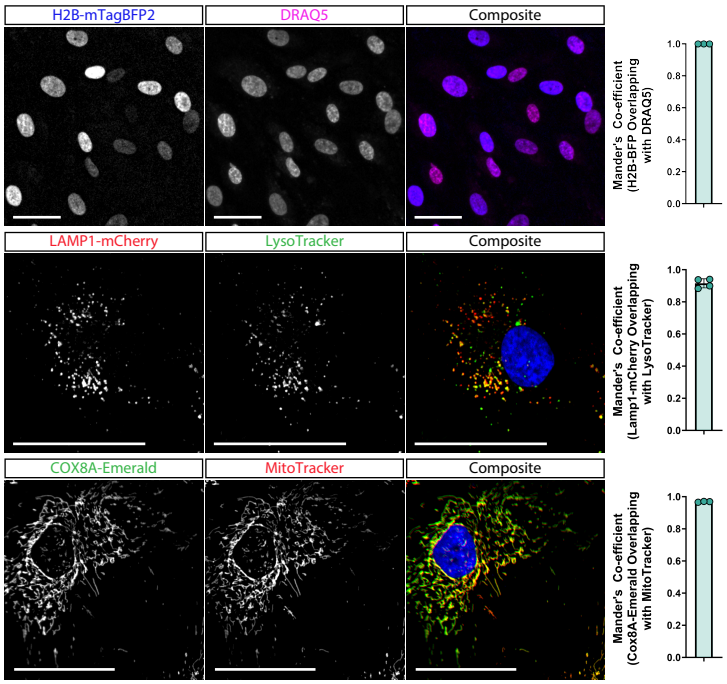

D.

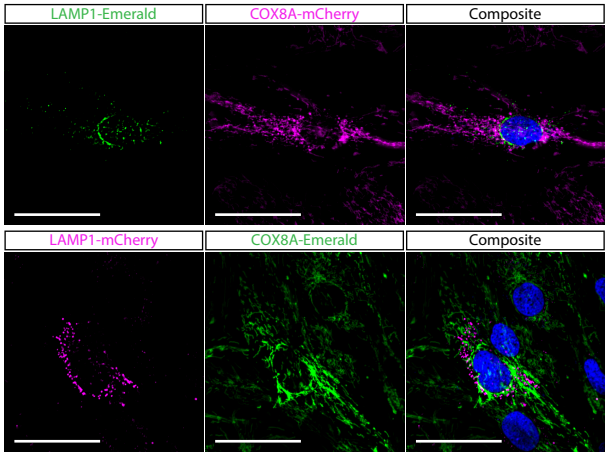

Figure 2

A.

B.

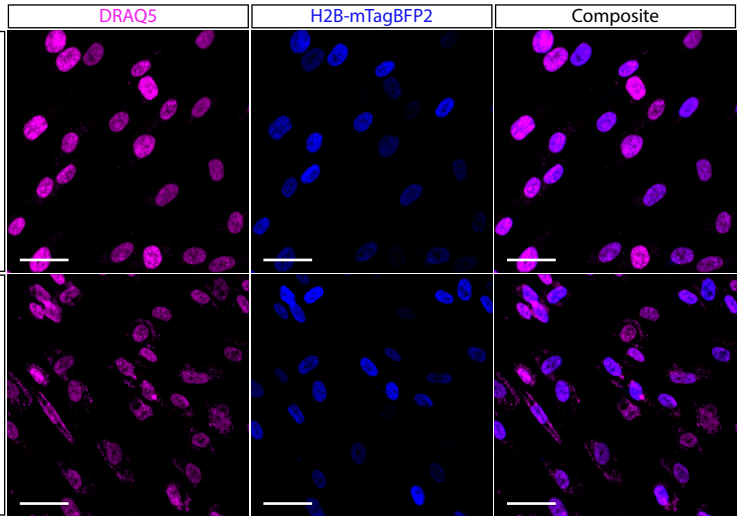

C.

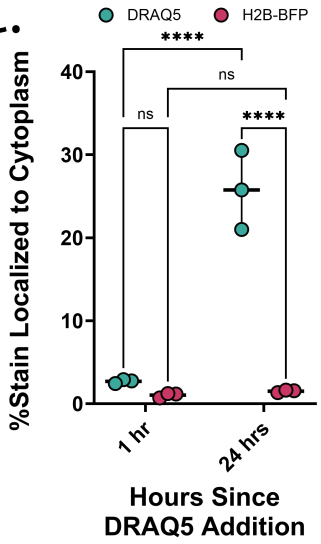

D.

E.

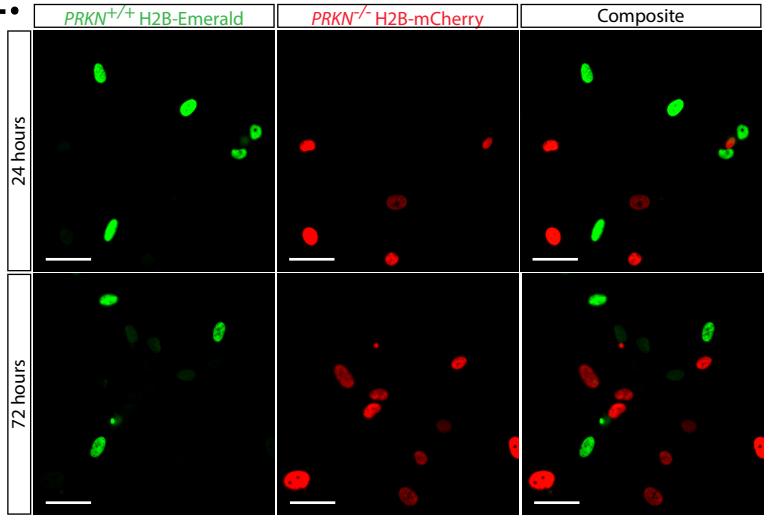

F.

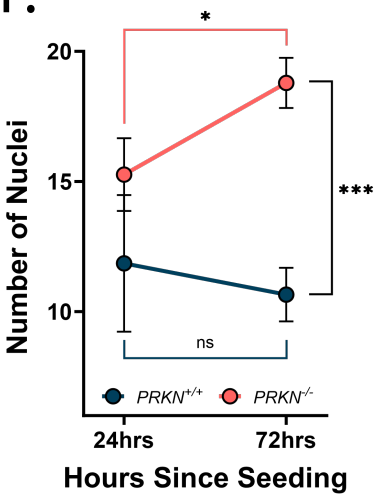

Figure 3

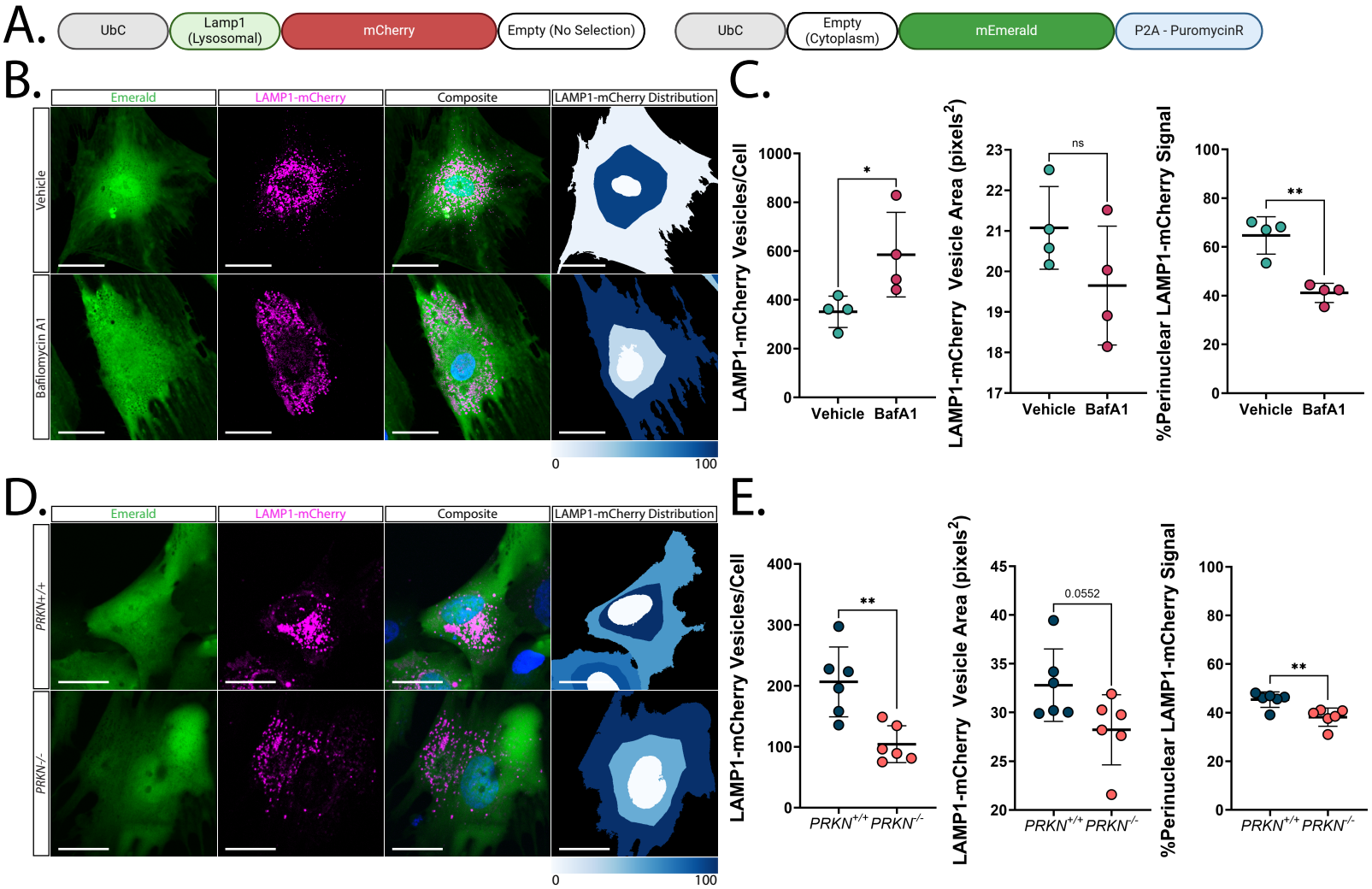
A.
UbC
Lamp1 (Lysosomal)
mCherry
Empty (No Selection)
UbC
Empty (Cytoplasm)
mEmerald
P2A - PuromycinR
B.
Emerald
LAMP1-mCherry
Composite
LAMP1-mCherry Distribution
Vehicle
Bafilomycin A1
0
100
C.
LAMP1-mCherry Vesicles/Cell
Vehicle
BafA1
LAMP1-mCherry Vesicle Area (pixels²)
ns
%Perinuclear LAMP1-mCherry Signal
D.
Emerald
LAMP1-mCherry
Composite
LAMP1-mCherry Distribution
PRKN+/+
PRKN-/-
0
100
E.
LAMP1-mCherry Vesicles/Cell
LAMP1-mCherry Vesicle Area (pixels²)
0.0552
%Perinuclear LAMP1-mCherry Signal
PRKN+/+
PRKN-/-

Figure 4

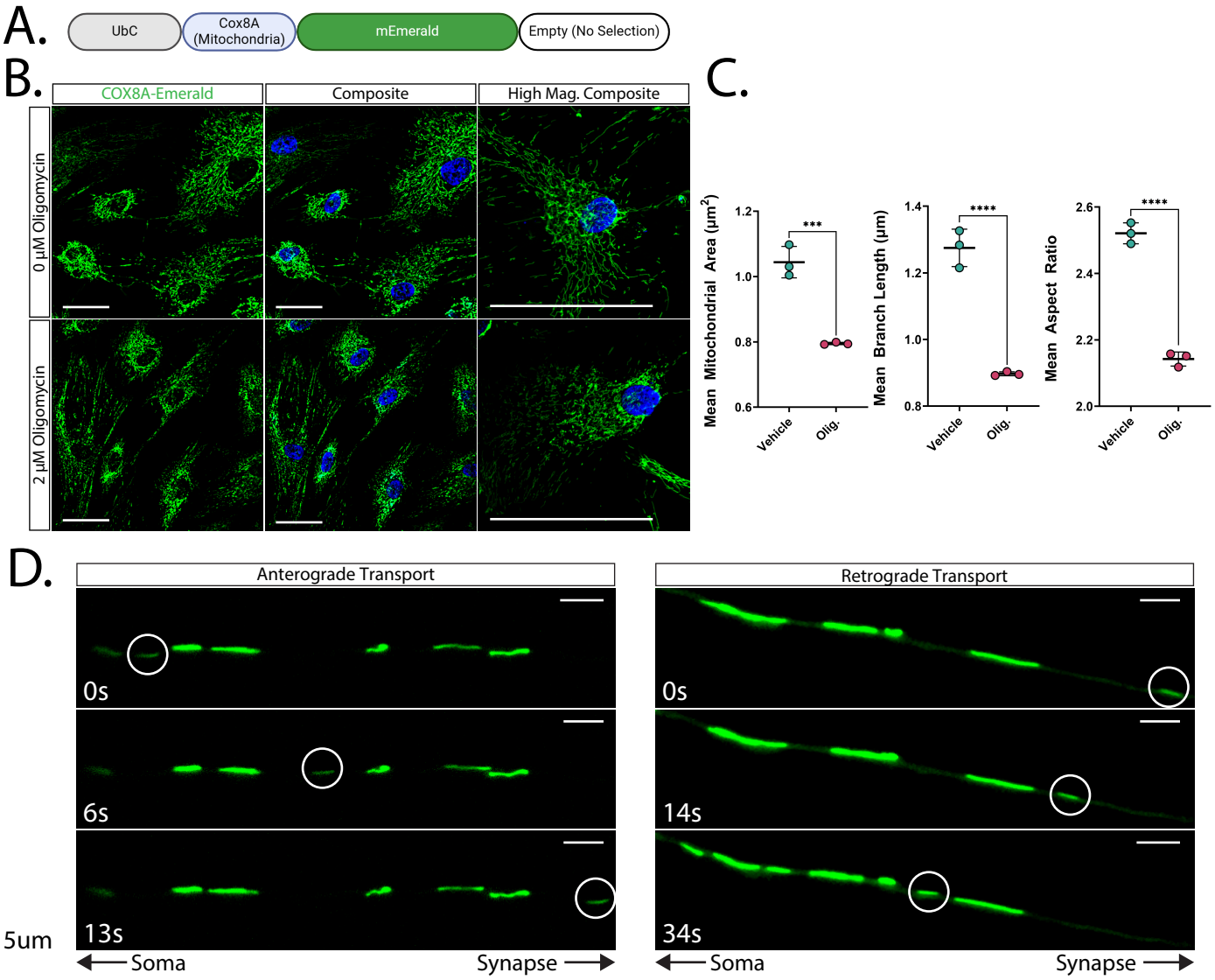
A.
UbC
Cox8A (Mitochondria)
mEmerald
Empty (No Selection)
B.
COX8A-Emerald
Composite
High Mag. Composite
0 µM Oligomycin
2 µM Oligomycin
C.
Mean Mitochondrial Area (µm²)
Mean Branch Length (µm)
Mean Aspect Ratio
Vehicle
Olig.
D.
Anterograde Transport
Retrograde Transport
0s
6s
13s
14s
34s
5um
Soma
Synapse

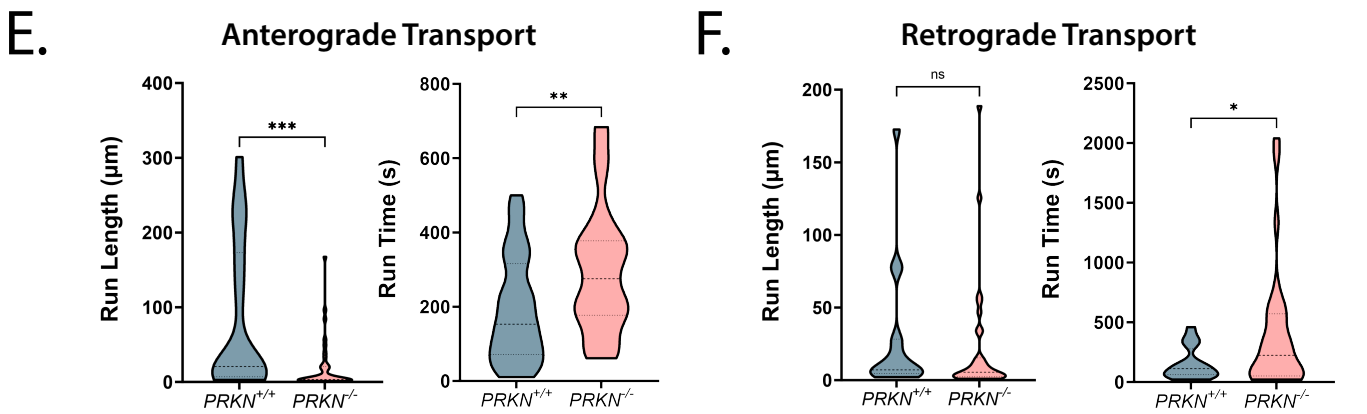
E.
Anterograde Transport
Run Length (µm)
Run Time (s)
PRKN+/+
PRKN-/-
F.
Retrograde Transport
ns

Figure 5

A.

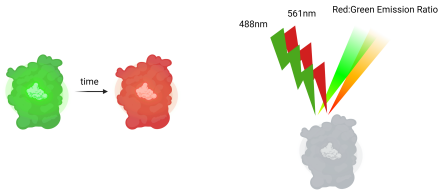

B.

C.

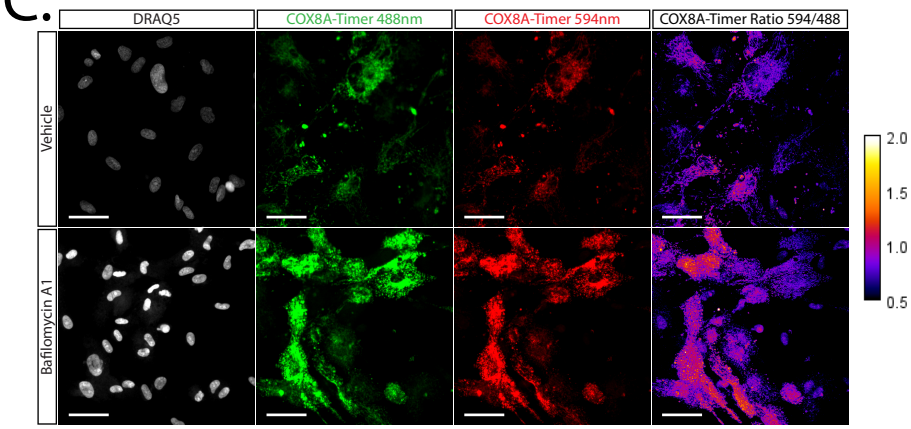

D.

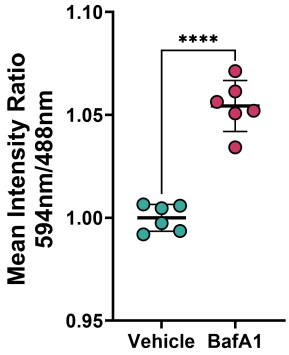

E.

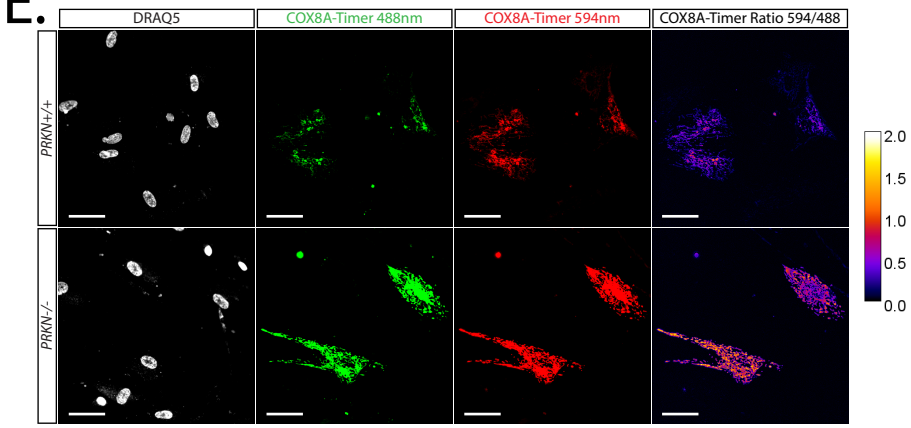

F.

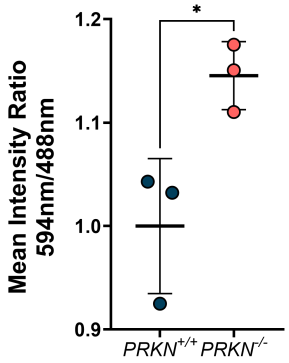

G.

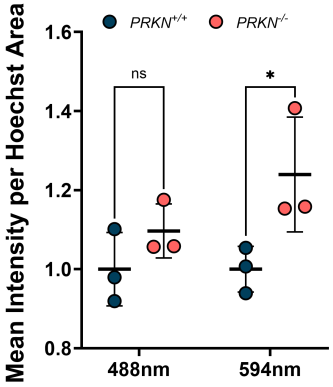

Figure 6

A.

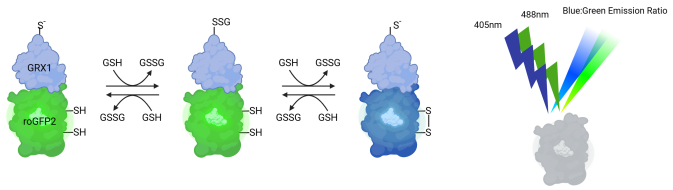

B.

C.

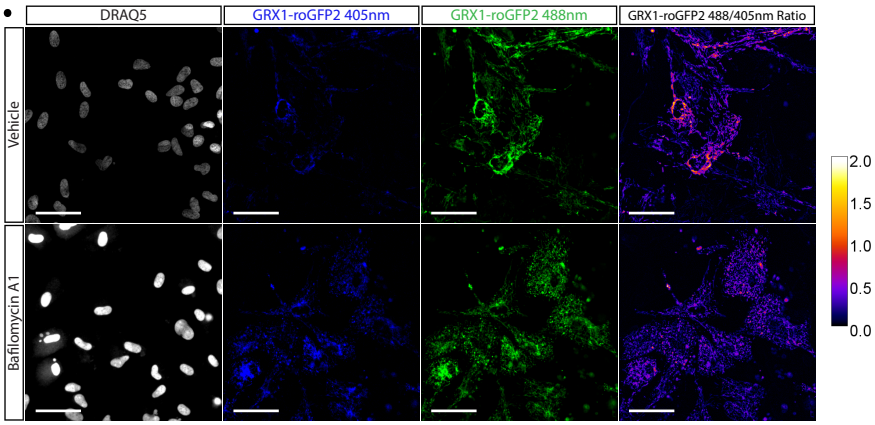

D.

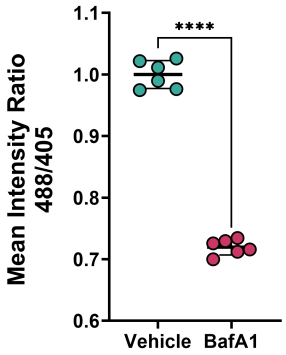

E.

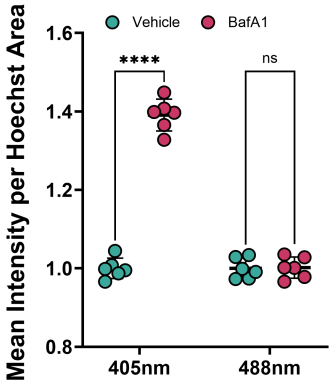

F.

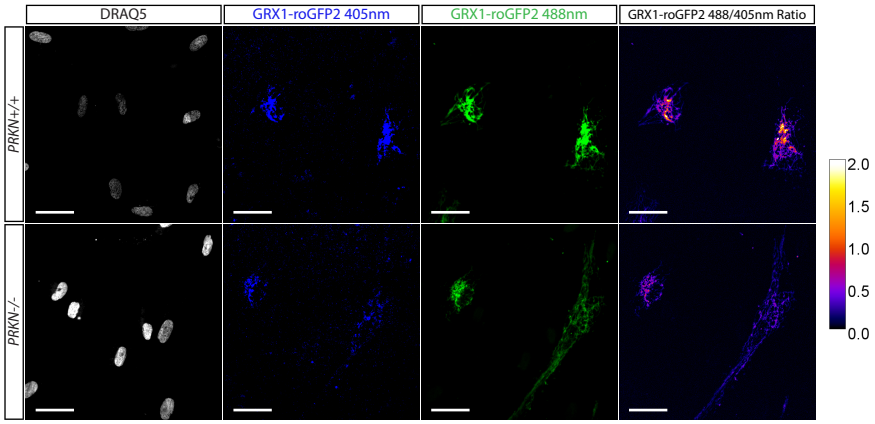

G.

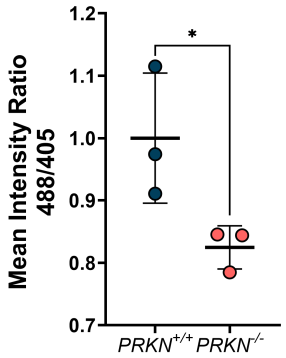

Figure S1

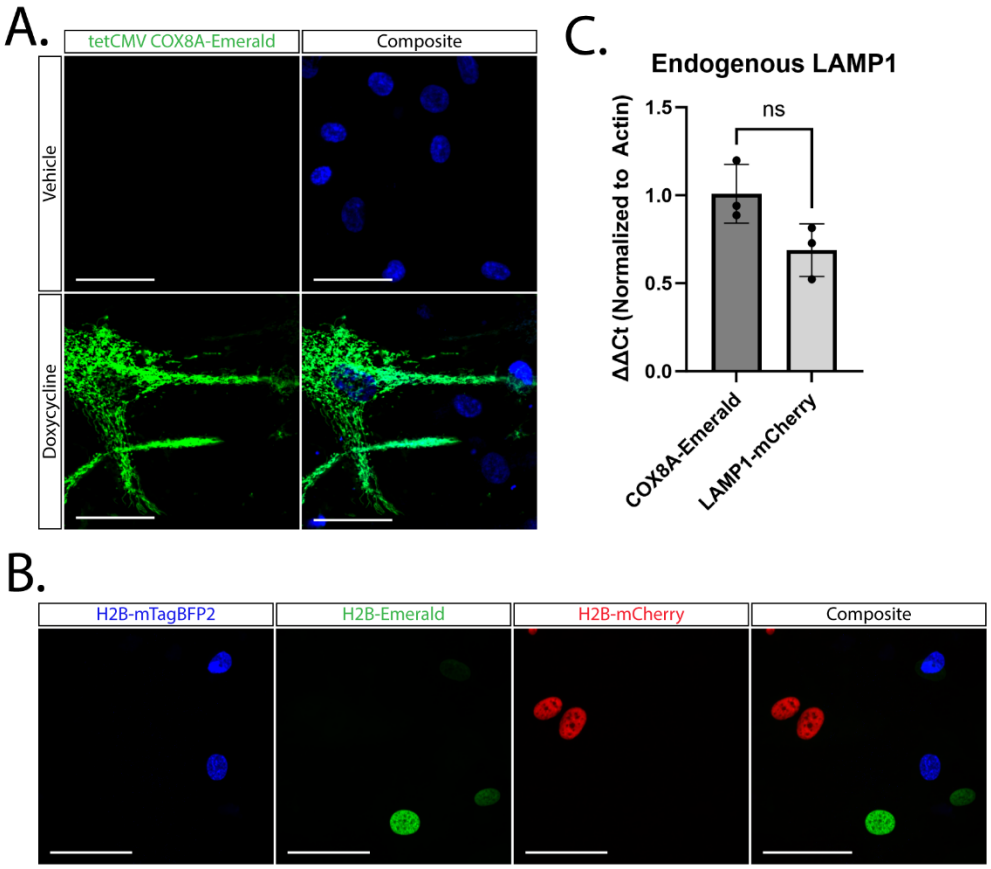

Fig. S1: GEM-SCOPe supports a diversity of modifications and applications (A) Representative images of astrocytes expressing COX8A-Emerald under the control of a doxycycline inducible promoter. Astrocytes were treated with a vehicle (DMSO; top) or doxycycline (bottom) for 72 hours. Nuclei were stained with Hoechst33342. **(B)** qPCR for endogenous *LAMP1* on RNA from astrocytes transduced with a virus localized to the lysosome (LAMP1-mCherry) or a virus not localized to the lysosome (COX8A-Emerald). qPCR primers were designed to amplify a sequence of *LAMP1* that is not included in the lentivirus to only quantify endogenous *LAMP1* levels. Bars represent mean and error bars represent standard deviation (n = 3 independent transductions). **(C)** Representative images of a mixed population of astrocytes with nuclei expressing different H2B-fusion fluorophores. Astrocytes were transduced with a single lentivirus and then plated together. Scale bar = 50 μm.

Figure S2

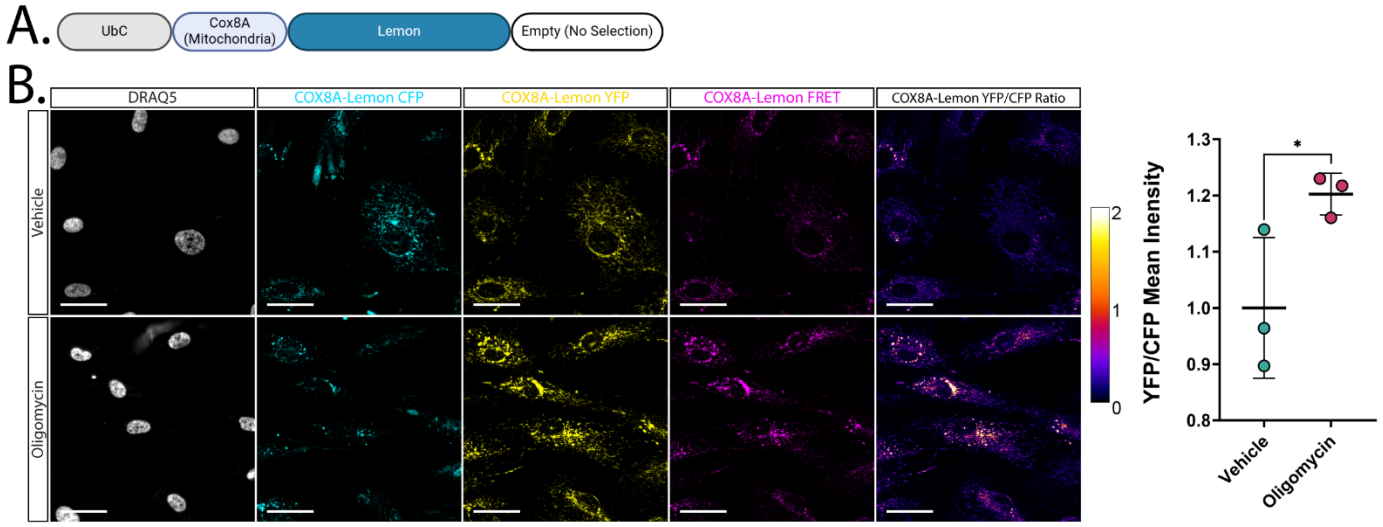

Fig. S2: Mitochondrial pH sensor measures disrupted mitochondrial membrane potential Schematic of the lentiviral construct used in the following panels localizing Lemon, a pH responsive fluorophore, to the mitochondria with the targeting sequence of COX8A. Lemon undergoes Forster Resonance Energy Transfer (FRET) under alkaline conditions. **(B)** Representative images of astrocytes transduced with COX8A-Lemon and treated with a vehicle (DMSO; top) or 2 μM oligomycin (bottom) for 24 hours. Images were acquired with a 455nm-excitation laser and a 515-excitation laser. Far right: ratiometric representation of the emission in the yellow channel divided by the emission in the cyan channel and then pseudo colored so that orange, yellow and white indicate more relative yellow emission (more alkaline) while black and purple represent more cyan emission (more acidic). Nuclei were stained with DRAQ5. Scale bars = 50 μm. **(C)** Quantification of the ratio of yellow emission to cyan emission in astrocytes expressing COX8A-Lemon and treated with DMSO or oligomycin. Central bars represent mean and error bars represent standard deviation (n = 3; each replicate is an average 36 images).

Figure S3

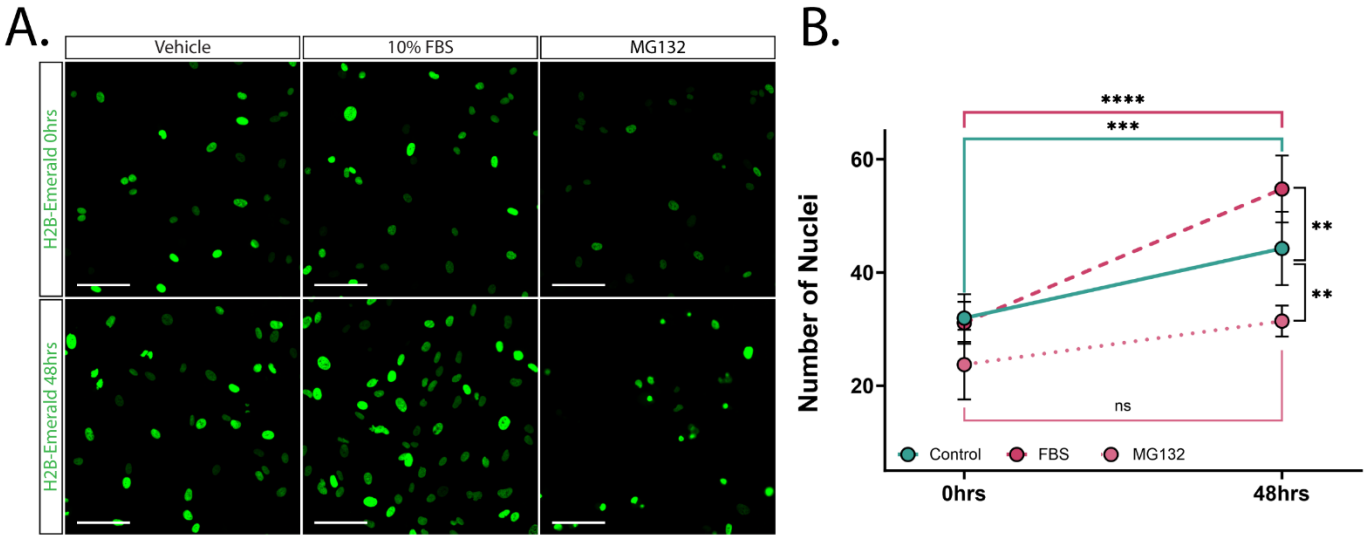

Fig. S3: Astrocyte proliferation is activated by FBS and inhibited by MG-132 (A) Representative images of astrocytes transduced with H2B-Emerald lentivirus after 0 hrs (top) or 48 hrs (bottom) of treatment with a vehicle (DMSO; left), 10% fetal bovine serum (FBS; middle), or MG132 (right). Scale bars = 50 µm. **(B)** Quantification of number of H2B-Emerald nuclei per image field 0 hours and 48 hours after treatment. Dots represent mean values and error bars represent standard deviation (n = 6 (n = 3 for MG-132 treatment) per time point; each replicate is an average over 25 images). Scale bars = 50 µm. All images were acquired on the CX7 HCS platform with a 20x objective lens.

Figure S4

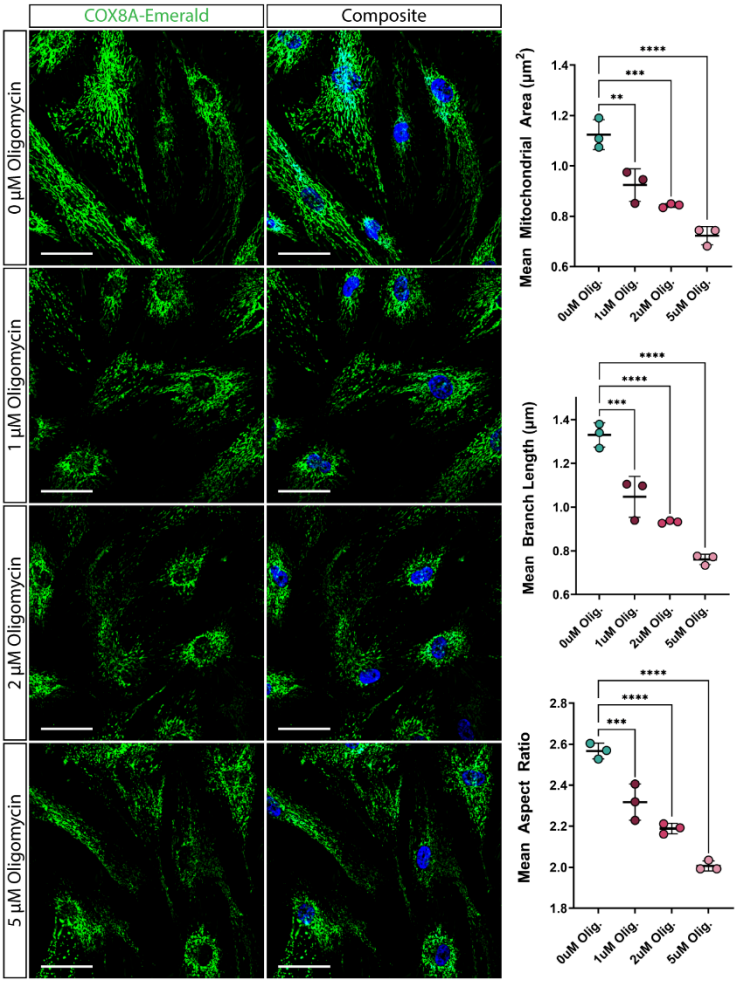

Fig. S4: Mitochondrial fragmentation exhibits a dose dependent response to oligomycin-induced stress **(A)** Representative images of astrocytes transduced with COX8A-Emerald and treated with a vehicle (DMSO), 1µM, 2 µM, or 5 µM oligomycin for 4 hours. Nuclei were stained with Hoechst33342. Scale bars = 50 µm **(B)** Quantification of mitochondrial features indicative of mitochondrial network fragmentation: mean area, perimeter, aspect ratio, number of branches, branch length, and number of branch endpoints. Central bars represent mean and error bars represent standard deviation (n = 3; each replicate is an average over 36 images).

Plasmid Name	AddGene Cat#	Localization	Fluorophore	Antibiotic Resistance	Relevant Figures
pFUW H2B-mTagBFP2-p2A-PuroR		Nucleus	mTagBFP2	Puromycin	1, 2, S1, S3
pFUW H2B-Emerald-p2A-PuroR		Nucleus	Emerald	Puromycin	2, S1
pFUW H2B-mCherry-p2A-PuroR		Nucleus	mCherry	Puromycin	2, S1
pFUW LAMP1Sig-Emerald		Lysosome	Emerald	NA	1, 3
pFUW LAMP1Sig-mCherry		Lysosome	mCherry	NA	1
pFUW COX8ASig-Emerald		Mitochondria	Emerald	NA	1, 4, S5
pFUW COX8ASig-mCherry		Mitochondria	mCherry	NA	1
pFUW PuroR-P2A-COX8ASig-Timer		Mitochondria	Timer	Puromycin	5
pFUW COX8ASig-Lemon		Mitochondria	Lemon	NA	S2
pFUW mito-GRX1-roGFP2		Mitochondria	roGFP2	NA	6
pFUW mTagBFP2		NA	mTagBFP2	NA	NA
pFUW Emerald		NA	Emerald	NA	NA
pFUW mCherry		NA	mCherry	NA	NA
pFUW mTagBFP2-P2A-PuroR		NA	mTagBFP2	Puromycin	NA
pFUW Emerald-P2A-PuroR		NA	Emerald	Puromycin	3
pFUW mCherry-P2A-PuroR		NA	mCherry	Puromycin	NA
pFUW mTagBFP2-P2A-NeoR		NA	mTagBFP2	Neomycin	NA
pFUW Emerald-P2A-NeoR		NA	Emerald	Neomycin	NA
pFUW mCherry-P2A-NeoR		NA	mCherry	Neomycin	NA

Table S1: A list of all plasmids generated in this study. Details for all plasmids, including subcellular localization, fluorophore, antibiotic resistance, and in which figure each plasmid was used. More plasmids were generated as part of GEM-SCOPe than used in the final publication, and these are also included here and available on Addgene.

Video S1: Mitochondrial axonal transport in *PRKN*$^{+/+}$ and *PRKN*$^{-/-}$ human iPSC derived neurons

Representative videos of COX8A-Emerald labeled mitochondria moving within neuronal axons over the course of 1 hour. Images were taken every 10 seconds and sped up 70x. Scale bar = 25 μm.